A&A 449, 171–192 (2006)
DOI: 10.1051/0004-6361:20054169

Astronomy & Astrophysics

X-ray emission from radiative shocks in type II supernovae

T. K. Nymark, C. Fransson, and C. Kozma

Stockholm Observatory, AlbaNova University Center, 106 91 Stockholm, Sweden
e-mail: tanja@astro.su.se

Received 7 September 2005 / Accepted 21 October 2005

ABSTRACT

The X-ray emission from the circumstellar interaction in type II supernovae with a dense circumstellar medium is calculated. In type IIL and type IIn supernovae, mass loss rates are generally high enough for the region behind the reverse shock to be radiative, producing strong radiation, particularly in X-rays. We present a model for the emission from the cooling region in the case of a radiative reverse shock. Under the assumption of a stationary flow, a hydrodynamic model is combined with a time-dependent ionization balance and multilevel calculations. The applicability of the steady state approximation is discussed for various values of the ejecta density gradient and different sets of chemical composition. We show how the emerging spectrum strongly depends on the reverse shock velocity and the composition of the shocked gas. We discuss differences between a spectrum produced by this model and a single-temperature spectrum. Large differences are found especially for the line emission, which can seriously affect abundance estimates. We also illustrate the effects of absorption in the cool shocked ejecta. The applicability of our model to various types of supernovae is discussed.

Key words. stars: supernovae: general – stars: circumstellar matter – X-rays: supernovae – hydrodynamics – shock waves – atomic processes

1. Introduction

For most type IIL (type II linear) and type IIn (type II narrow line) supernovae, the emission at late times is dominated by the interaction between the supernova ejecta and the circumstellar medium. The collision between the two creates two shocks; one moving outward into the circumstellar medium and a reverse shock that moves backward into the ejecta (Fig. 1). Because of the high temperatures involved, most of the emission from the interaction region is radiated as X-rays. The strong emission heats and ionizes the circumstellar medium and ejecta, leading to line emission in the optical and UV (Fransson 1984; Chevalier & Fransson 1994, hereafter CF94). This can then act as probes of the ejecta and the shock. Another characteristic feature of the interaction is strong radio emission caused by synchrotron emission behind the outer shock (e.g., Sramek et al. 2003). A review of circumstellar interaction in supernovae is given by Chevalier & Fransson (2003).

Chevalier (1982a,b) proposed circumstellar interaction as an explanation of the observed radio light curves of SN 1979C and SN 1980K, and used a self-similar formulation to analyze the effects of interaction between supernova ejecta and the ambient medium. Different mechanisms for production of X-rays were also discussed. In Fransson (1984) the X-ray emission from the reverse and circumstellar shocks was discussed in some detail. In particular, it was argued that in most cases the reverse shock would be radiative, which we exploit in this paper. This also has the consequence that a cool, dense shell will form between the two shocks, which is important for both the X-ray and optical emission. A detailed study of the effects of circumstellar interaction in type II supernovae was made by Chevalier & Fransson (1994), while the specific case of SN 1993J was investigated by Fransson et al. (1996, hereafter FLC96), as well as by Suzuki & Nomoto (1995).

Radiative shocks in supernova remnants were first modeled by Cox (1972). Later, improved models were made by Raymond (1979), Dopita (1976, 1977), and others. Because of the lower densities, the shocks are, however, only radiative for velocities $\lesssim$200 km s^{-1}, substantially lower than the velocities studied in the present paper. High density models, suitable for active galactic nuclei (AGN) and young supernova remnants, were made by Plewa & Różyczka (1992) and Plewa (1993, 1995). These models are, however, mainly concerned with hydrodynamics, and offer a simplified treatment of the emergent spectra.

The goal of this paper was therefore to develop a model for the X-ray emission from the reverse shock. This combines the hydrodynamic structure with a spectral code that, by including updated atomic data and multi-level solutions to most ions, can model the line emission in greater detail than has been done before.

In Sect. 2 we give a brief summary of the most important observations of circumstellar interaction and, in particular, of X-ray observations. Our model is described in Sects. 3 through 6, while Sect. 7 describes the results of our calculations, including the contribution from the circumstellar shock. The conclusions are then summarized in Sect. 8.

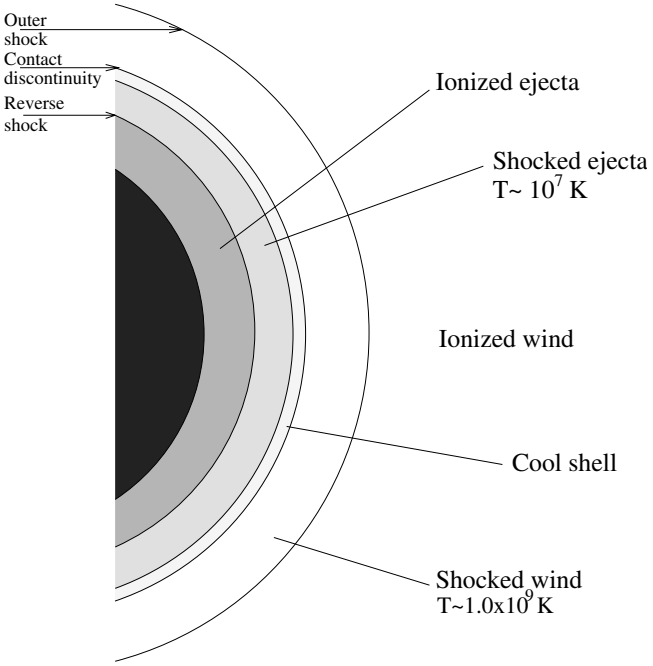

Fig. 1. Schematic picture of the different regions in the interaction of supernova ejecta with the progenitor wind. The figure is not to scale. The contact discontinuity between the shocked wind and shocked ejecta is Rayleigh-Taylor unstable.

2. X-ray emission from supernovae

The main observational indications of circumstellar interaction are (i) the detection of narrow optical and UV emission lines from ionized circumstellar gas, (ii) broad, box-like emission lines from ejecta ionized by radiation from the interaction region, and (iii) a wavelength-dependent turn-on of the observed radio emission. The last is explained as a result of either free-free absorption or synchrotron self-absorption. Another effect of circumstellar interaction is that the supernova displays a flat optical light curve at late epochs, long after the emission caused by radioactive decay has faded away. For type IIn supernovae circumstellar interaction already dominates the optical spectrum from early epochs. We refer to Filippenko (1997) for a review of the optical observations.

Besides the radio emission, the X-rays show the clearest evidence of circumstellar interaction. Because the X-ray emission is the focus of this paper, we will briefly review the observational evidence for this. Until now, ∼24 supernovae have been detected in X-rays, and for ∼10 of these the data are good enough to be studied in detail. We will concentrate on those for which good data exist, and where circumstellar interaction is thought to be important. Comprehensive reviews of the existing X-ray observations of supernovae can be found in Schlegel (1995) and Immler & Lewin (2002)[1].

The first supernova to be detected in X-rays was SN 1980K, which was observed by the Einstein satellite 35 days after outburst (Canizares et al. 1982). At the time of the next observation at 82 days, the emission had decayed by at least a factor of two. The emission was found to be rather soft with $kT \sim 0.5$ keV, but no spectra were obtained. Also SN 1979C was observed with Einstein at early epochs, but no source was seen (Panagia et al. 1980). After ∼16 years it was, however, detected as a strong source by ROSAT (Immler et al. 1998). It was observed by the ASCA satellite in 1997 (Ray et al. 2001) and by Chandra in 1999 and 2000 (Kaaret 2001), with a roughly constant X-ray flux in the period of 16–20 years after outburst. The emission was found to be soft, and likely to originate in the shocked ejecta. The reason for the absence of strong X-rays at early epochs is most likely absorption by the cool, dense shell formed by the reverse shock (CF94).

The type IIn SN 1986J in NGC 891 was observed with ROSAT and ASCA from nine to thirteen years after outburst (Houck et al. 1998). During this period it was found to have a fast decline in the X-ray emission, with $L_x \propto t^{-2}$. From the ASCA observations, it was found to have a rather hard spectrum ($kT \sim 5-7$ keV) with a clear Fe K emission line at 6.7 keV, with a width $< 20\,000$ km s^{-1}.

The first supernova to be identified through its X-ray emission was the type IIn SN 1978K. Strong radio and optical emission had been detected earlier (Ryder 1993; Dopita & Ryder 1990), but with the detection of X-rays by ROSAT in 1992 (Ryder 1993) it was identified as a supernova. Extensive observations in radio, optical, UV, and X-rays were carried out in the late 1990s; then observations by Newton-XMM in October 2000 and by Chandra two years later indicated a constant X-ray flux over the past decade (Schlegel et al. 2004). In the early X-ray spectra, no emission lines were found, but in the Chandra data lines from Si are evident.

The best observed case of circumstellar interaction is SN 1993J in M 81. Since its discovery in March 1993, it has been extensively studied in all wavebands; SN 1993J showed signs of circumstellar interaction early on, first through the detection of radio emission on day 5 (Weiler et al. 1993) and shortly thereafter through X-ray observations. The first X-ray detection was made by ROSAT as early as 6 days after discovery (Zimmerman et al. 1994), and the first observation by ASCA came two days later. The early ASCA observations showed a strong Fe K line at 6.7 keV with a width of 0.3 ± 0.3 keV, which faded within weeks after the explosion (Kohmura et al. 1994; Uno et al. 2002). Both ROSAT and ASCA observations showed a hard spectrum during the first two months. This was confirmed by OSSE observations on Compton/GRO, where hard X-ray emission with $kT \sim 50-150$ keV was detected in two observations, 9.9–15.4 days after explosion and again between days 23.7–36.9 (Leising et al. 1994). Three months after explosion it was too weak to be observed by OSSE. When it was re-observed by ASCA and ROSAT after six months, a soft component was found to dominate the spectrum. This transition from a hard to a soft spectrum was explained by FLC96 as a result of decreasing optical depth in the cool shell between the two shocks, which allows the soft X-rays from the reverse shock to escape.

Very late Chandra observations on day 2594 yielded a detailed spectrum of SN 1993J in the 0.3–8.0 keV band

[1] A complete list of the X-ray supernovae may be found at `http://lheawww.gsfc.nasa.gov/users/immler/supernovae_list.html`

(Swartz et al. 2003). This spectrum showed evidence of Fe L emission, as well as emission from H-like Mg and Si and from He-like Mg, Si, and S. This is taken by Swartz et al. to indicate the presence of two low-temperature components, while the high energy ($\gtrsim$1.5 keV) continuum emission is thought to point to a high-temperature component as well.

The type IIn SN 1995N was detected by ROSAT in 1996. The explosion date is unknown, but Fransson et al. (2002) argue that a likely explosion date was July 1994, based on the spectrum. It was observed by ROSAT in 1996 and 1997, by ASCA in 1998 (Fox et al. 2000), and by Chandra in 2004 (Chandra et al. 2005). The X-ray luminosity was found to decline between the first two observations. Fox et al. (2000) found that the luminosity increased again by a factor of two from 1997 to 1998, although reanalysis by Chandra et al. (2005) of the ASCA observations indicates that the source was contaminated and that both the ASCA and Chandra observations are consistent with a linear decline in the X-ray luminosity. Chandra et al. (2005) also find clear evidence of Ne line emission around 1 keV.

The other well-observed type IIn SN 1998S in NGC 3877 was discovered at an early phase, and has been studied well at all wavelengths. It was observed by Chandra on five occasions from day 678 to day 1324 (Pooley et al. 2001). A number of emission lines from metals were observed at energies above 1 keV, among them lines from Ne, Si, S, and Fe. The strengths of the observed lines were claimed to indicate a high overabundance of the metals with respect to solar values. This would imply that the observed X-ray emission mainly comes from the shocked oxygen core. In this case the heavy elements must be mixed out to a high velocity, possibly caused by an aspherical explosion (Pooley et al. 2001). The abundance analysis is, however, based on a one-temperature model of the spectrum. In Sect. 7.7 we show that this assumption is highly questionable.

The first type IIP supernova to be detected both in X-rays and radio, SN 1999em, was detected by Chandra three days after discovery, and was observed a total of seven times in a period of almost two years. During this period the spectrum softened from $a \sim 5$ keV spectrum to $a \sim 1$ keV spectrum. Pooley et al. (2001) modeled the X-ray emission as resulting from interaction between supernova ejecta and the wind of a red supergiant, and found that the X-ray emission agrees well with this, and that both shocks were adiabatic.

The most recent X-ray supernova is the type IIP SN 2004dj, which was detected by Chandra in August 2004, most likely two months after explosion. It was found to have a temperature of $kT \sim 7$ keV, and nearly three times the luminosity of SN 1999em (Pooley & Lewin 2004). Modeling of type IIP supernovae is discussed in detail by Chevalier et al. (2005).

3. Hydrodynamics

3.1. Progenitor wind

The immediate surroundings of the exploding star consist of the stellar wind of the progenitor. The density of a wind with constant mass loss rate and velocity drops as r^{-2}, but the wind parameters depend on the evolutionary state of the star. On the main sequence, the star is a blue supergiant with a fast wind. It then evolves to become a red supergiant with a correspondingly slow and dense wind, with a mass loss rate of $\dot{M} \sim 10^{-6}$–$10^{-4}\ M_\odot\ \mathrm{yr}^{-1}$ and a velocity of $v_\mathrm{w} \sim 5$–$50\ \mathrm{km\,s}^{-1}$ (e.g., Salasnich et al. 1999). Most massive stars explode in this stage as supernovae. Stars that are more massive than $\sim$22 $M_\odot$ (Meynet & Maeder 2003) may, however, evolve back to the blue and become Wolf-Rayet stars or, in some cases, end their lives as blue supergiants.

As the star evolves, the wind will create an onion-like structure of circumstellar gas, with dense shells alternating with low density shells. In some stages the progenitor may undergo pulsations (Heger et al. 1997), which could result in a wind with a density differing from $\rho \propto r^{-2}$. The circumstellar medium can also be modified by mass loss in a binary system, as might have been the case for SN 1993J (e.g., Suzuki 1994; Suzuki & Nomoto 1995; Nomoto et al. 1995). Because of this, the assumption that the density drops as distance squared may not always hold. A more general description of the wind density is therefore

$$\rho_\mathrm{w} = \frac{\dot{M}}{4\pi R_*^2 v_\mathrm{w}} \left(\frac{R_*}{r}\right)^s, \tag{1}$$

where R_* is a reference radius. For $s = 2$ this reduces to the expression for a steady wind. There are few cases of deviations from $s = 2$ winds (see Fransson & Björnsson 2005 for a discussion). In some cases, the supernova may, however, interact with either clumpy winds or shell-like structures, for which s may differ from 2 (see Sect. 3.3).

3.2. Ejecta

The unshocked supernova ejecta are assumed to expand freely, so that the position of a specific mass element can be expressed as $R(t) = Vt$, where the velocity V is constant. The structure of the ejecta reflects both the structure of the progenitor and the physics of the explosion.

A useful approximation for the density structure of the outer ejecta is

$$\rho_\mathrm{ej} = \rho \left(\frac{t}{t_0}\right)^{-3} \left(\frac{V_0 t}{r}\right)^\eta, \tag{2}$$

where η is the power law index characterizing the outer ejecta. Analytical ejecta models by Matzner & McKee (1999) indicate that $\eta = 11.9$ for a red supergiant progenitor and $\eta = 10.1$ for a blue supergiant progenitor. For this to be valid, the progenitor structure has to be close to a polytrope of index 3/2 (convective envelope) or 3 (radiative envelope), respectively, which does not always hold. In particular, the models of Matzner & McKee do not apply to superadiabatic regions, which can be present in certain progenitors. This may have been the case for SN 1993J (Nomoto et al. 1995).

In more detailed hydrodynamical explosion models, the power law index η is usually in the range 7–12, but can be as high as $\sim$20, as is the case in the ejecta models of SN 1993J. Evolutionary progenitor models (Shigeyama & Nomoto 1990; Woosley & Weaver 1995) indicate that a power law structure

is a good approximation for the outer layers, and to some extent also in the inner parts, albeit with a different value for the power law index, η. Roughly speaking, most one-dimensional models show a steep inner power law, a shallow middle part, and a steep outer part, although there is considerable structure, particularly in the inner parts. However, hydrodynamic instabilities at especially the H/He interface, as well as the He/O core, can modify the structure appreciably (Müller et al. 1991; Iwamoto et al. 1997; Kifonidis et al. 2003).

During the first weeks or months, the reverse shock passes through the outermost steep part and enters the shallower gradient toward the middle. The shallow part is traversed quickly, and eventually the shock enters the inner steep part. As the shock moves into a region with a different density slope, the X-ray spectrum will change. The time at which this spectral change occurs could help constrain the explosion models. We will discuss this in more detail in a later paper.

3.3. Interaction region

Chevalier (1982a) found a self-similar solution for the interaction between supernova ejecta and a stationary medium, which provided a complete solution to the physical quantities of the two shocks (see also Nadyozhin 1985). The main parameters are the power law exponents, η and s, of the ejecta and wind densities, the mass loss parameter $\dot{M}/v_{\rm w}$, and the shock velocity (or equivalently the total energy).

These relations can be simplified further if one assumes that the interaction shell is very thin compared to its radius (the thin shell approximation), which is usually an adequate approximation. This becomes exact in the limit of strong radiative cooling, which is the case for the reverse shocks discussed in this paper. The circumstellar shock is in general, however, adiabatic. A similarity solution describing this case is discussed in CF94. In the following, the subscript "0" refers to quantities immediately behind the reverse shock, "rev" refers to parameters of the shock itself, while the subscript "cs" refers to the circumstellar shock.

The density and temperature behind the reverse shock can in the thin shell approximation be written as (FLC96)

$$\rho_0 = \frac{(\eta-3)(\eta-4)}{(3-s)(4-s)}\rho_{\rm cs} \tag{3}$$

$$T_0 = \frac{\mu}{\mu_{\rm cs}}\frac{(3-s)^2}{(\eta-3)^2}T_{\rm cs} = 2.27\times10^9\mu\frac{(3-s)^2}{(\eta-s)^2}V_4^2 \quad {\rm K} \tag{4}$$

where μ is the mean mass per particle (i.e., electrons plus ions) behind the reverse shock, and $\mu_{\rm cs}$ is the corresponding value behind the circumstellar shock. The density behind the outer shock is related to the wind density by $\rho_{\rm cs} = 4\rho_{\rm w}$. Setting $r = R_{\rm s} = V_{\rm ej}t$ in Eq. (1), we can express the post-shock ion number density as

$$n_0 = 1.2\times10^{38}\frac{(\eta-3)(\eta-4)}{(3-s)(4-s)}\frac{\tilde{A}_*}{\mu_{\rm A}V_{\rm ej}^s t^s}R_*^{s-2} \quad {\rm cm}^{-3}, \tag{5}$$

where $\mu_{\rm A}$ is the mean atomic weight, and we have defined $\tilde{A}_* = \dot{M}_{-5}/v_{\rm w_1} = (\dot{M}/10^{-5}\ M_\odot)/(v_{\rm w}/10\ {\rm km\,s^{-1}})$. Note that $\tilde{A}_* = 100\,A_*$, where A_* was defined by Chevalier & Li (1999) for parameters that are typical of a Wolf-Rayet wind. Then $R_{\rm s}$ is the radius of the interaction region, which we here take to be the same as the position of the reverse shock, and $V_{\rm ej}$ is the maximum velocity of the ejecta, i.e., the velocity of the ejecta at the reverse shock front. Note that the radius of the circumstellar shock, $R_{\rm cs}$, is a factor 1.2–1.3 larger than $R_{\rm s}$ (CF94).

The temperature behind the circumstellar shock is

$$T_{\rm cs} = 2.27\times10^9\mu_{\rm cs}\frac{(\eta-3)^2}{(\eta-s)^2}V_4^2 \quad {\rm K}, \tag{6}$$

where $V_4 = V_{\rm ej}/10^4$ km s^{-1}. Values of μ and $\mu_{\rm A}$ are given in Table 1 for the different compositions considered in this paper. The composition of the circumstellar shock is the same as in the circumstellar medium, which we assume to be solar, with $\mu_{\rm cs} \approx 0.61$. The mass swept up by the outer shock front is

$$M_{\rm cs} = \frac{\dot{M}R_{\rm s}}{(3-s)v_{\rm w}}\left(\frac{R_{\rm s}}{r_0}\right)^{(2-s)}, \tag{7}$$

and the mass swept up by the reverse shock is

$$M_{\rm rev} = \frac{\eta-4}{4-s}M_{\rm cs}. \tag{8}$$

The velocity of the reverse shock is

$$V_{\rm rev} = \frac{3-s}{\eta-s}V_{\rm ej}, \tag{9}$$

which in combination with the shock jump condition gives the velocity of the post-shock gas

$$v_0 = \frac{V_{\rm rev}}{4} = \frac{(3-s)}{4(\eta-s)}V_{\rm ej}. \tag{10}$$

As an alternative to using a self-similar model, one that is dependent on the assumption that the ejecta density is a power law, $\rho \sim r^{-\eta}$, we have the option of using a more detailed, non-power law model for the ejecta as input. In this case we use the thin shell approximation to solve for the position of the shock, and consequently the density, temperature, and velocity of the ejecta at this position (see e.g. Chevalier & Fransson 2003). The post-shock values are then found from the shock jump conditions. Once the state of the post-shock gas has been found, the treatment of the interaction is the same in both cases, as described below.

An alternative scenario for the X-ray emission is one with shocks driven into dense circumstellar clumps (e.g. Chugai 1993). In this case the X-ray emission would originate in radiative shocks within each clump. The structure of the radiative shocks would, however, be the same as for the reverse shock considered here. An especially interesting case of this type is the ring collision of SN 1987A (Michael et al. 2002).

3.4. Reverse shock structure

The structure of the shocked ejecta behind the reverse shock is found by solving the conservation equations. If we reduce the

problem to one dimension, which is justified for a thin shock, and assume steady state, these equations reduce to

$$\frac{\mathrm{d}}{\mathrm{d}x}\left(n_{\mathrm{i}}v\right) = 0 \tag{11}$$

$$\frac{\mathrm{d}}{\mathrm{d}x}\left(\mu_{\mathrm{A}}m_{\mathrm{u}}n_{\mathrm{i}}v^2 + p\right) = 0 \tag{12}$$

$$\frac{\mathrm{d}}{\mathrm{d}x}\left[\left(\frac{1}{2}\mu_{\mathrm{A}}m_{\mathrm{u}}n_{\mathrm{i}}v^2 + \frac{p}{\gamma-1} + p\right)v\right] = \Lambda(T)n_{\mathrm{i}}n_{\mathrm{e}}, \tag{13}$$

where n_{i} is the ion number density and Λ the cooling rate. These equations may be solved to give the structure of the radiative shell, once the values immediately behind the shock are known. For the thin shell model the initial density and temperature are given by Eqs. (3) and (4), and the initial velocity by Eq. (10). The initial pressure is $p_0 = (n_{\mathrm{e},0} + n_0)kT_0$.

The model is specified by the density, temperature, and composition behind the shock. The initial value of the density depends on which structure we assume for the ejecta (see Sect. 3.3). Once the density structure is set, the pressure and velocity of each zone can be found from the continuity equations

$$v = n_0v_0n_{\mathrm{i}}^{-1} \tag{14}$$

$$p = \mu_{\mathrm{A}}m_{\mathrm{u}}n_0v_0^2\left(1 - \frac{n_0}{n_{\mathrm{i}}}\right) + p_0, \tag{15}$$

and the temperature is given by

$$\begin{aligned} T &= \frac{p}{k\left(n_{\mathrm{e}} + n_{\mathrm{i}}\right)} \\ &= \frac{1}{k(n_{\mathrm{e}} + n_{\mathrm{i}})}\left[\left(\mu_{\mathrm{A}}m_{\mathrm{u}}n_0v_0^2 + p_0\right) - \mu_{\mathrm{A}}m_{\mathrm{u}}\left(\frac{n_0v_0}{n_{\mathrm{i}}}\right)^2\right]. \end{aligned} \tag{16}$$

The position of each zone is found from Eq. (13), using the density as the independent variable to solve for $x(n_{\mathrm{i}})$,

$$x = \int_{n_0}^{n_{\mathrm{i}}} \frac{1}{\Lambda[T(n'), n']}\left[\frac{2A}{n'^5} + \frac{B}{n'^4}\right]\mathrm{d}n', \tag{17}$$

where Λ is the total cooling rate, and A and B are constants, determined by the initial values of density and velocity behind the reverse shock

$$A = -\frac{(\gamma+1)}{2(\gamma-1)}\left(\frac{\mu_{\mathrm{A}}}{\mu} - 1\right)\mu_{\mathrm{A}}m_{\mathrm{u}}(n_0v_0)^3, \tag{18}$$

$$B = \frac{\gamma}{(\gamma-1)}\left(\frac{\mu_{\mathrm{A}}}{\mu} - 1\right)\left(\mu_{\mathrm{A}}m_{\mathrm{u}}v_0^3 + v_0T_0\right). \tag{19}$$

We continue the calculations until the temperature falls below $\sim 10^5$ K. Below this temperature the contribution to the X-ray emission is negligible.

As the gas cools, the differential pressure between adjacent cooling regions causes instabilities, which can create secondary shocks within the cooling gas, particularly for high shock velocities (Chevalier & Imamura 1982; Plewa & Różyczka 1992; Plewa 1993, 1995; Dopita & Sutherland 1996; Sutherland et al. 2003). A complete treatment of this requires multidimensional hydrodynamical models. The specific case discussed in this paper was studied by Chevalier & Blondin (1995). Although the hydrodynamic structure can be severely affected, it is, however, likely that the time-averaged spectrum is close to that of a steady flow, as was indeed found by Innes (1992). As discussed by Sutherland & Dopita (1996), secondary shocks can nevertheless affect the line strengths of the lowest ionization species. This effect is of minor importance to us, since the lowest ionization stages have little or no impact on the X-ray emission. Dopita & Sutherland (1996) also conclude that limited spatial resolution in observational data has a more serious effect than neglecting thermal instabilities. Because several cooling cells and ranges of shock parameters are included in one beam, the effect of instabilities is reduced. This should certainly hold for the cases of interest here, where the size of each cooling cell is relatively small. Therefore, we conclude that neglecting instabilities in the cooling region is not likely to have serious implications for the computed spectrum. The main effect should be that there should be some spread in the reverse shock velocity. The spectrum may then be a superposition of several radiative shocks with different velocities. This will also be the case for a reverse shock receding into a clumpy ejecta, as seen in e.g. Cas A (Chevalier & Kirshner 1979; Chevalier & Oishi 2003; Fesen et al. 2006) and inferred for some supernovae, like SN 1995N (Fransson et al. 2002).

4. Chemical composition

The circumstellar shock sweeps up material lost by the star before the explosion, which should be close to solar composition for type II supernovae, although CNO burning may modify the relative abundances of C, N, and O for massive progenitors (e.g., Fransson et al. 2005). The reverse shock, on the other hand, propagates into the ejecta, sweeping up material that may have undergone nucleosynthesis. The composition of the ejecta varies with radius because of the successive burning stages in the progenitor, although hydrodynamical mixing may have modified this stratification. The mixing makes it more likely that enriched material will be encountered at higher velocities. As the reverse shock moves backward into the ejecta, it passes through regions of different composition. If the progenitor has already lost part or all of its hydrogen envelope, this may already occur during the early phases of the supernova. Examples are the type IIb SN 1993J and some type IIn supernovae, like SN 1995N.

To investigate the effects of composition on the spectrum, we calculated four models with the same temperature and maximum ejecta velocity, but different composition characteristics for the burning zones. One is for a solar composition, while the other three are characteristic of helium, carbon, and oxygen-dominated regions, respectively. Abundances of these three models were taken from the 4H47 model by Nomoto & Hashimoto (1988) and Shigeyama et al. (1994) and are listed in Table 1. The Ni abundances of the non-solar compositions, not given by the models, were estimated so that the Fe/Ni ratio would be the same as for the solar composition.

Table 1. Fractional abundances by number and atomic weights for the different compositions.

Element	Solar	Helium zone	Carbon zone	Oxygen zone
H	9.10×10^{-1}	–	–	
He	8.89×10^{-2}	9.82×10^{-1}	2.49×10^{-1}	2.36×10^{-10}
C	3.79×10^{-4}	1.24×10^{-2}	4.29×10^{-1}	4.53×10^{-3}
N	7.92×10^{-5}	–	–	–
O	6.29×10^{-4}	3.75×10^{-3}	3.10×10^{-1}	8.49×10^{-1}
Ne	8.89×10^{-5}	1.56×10^{-3}	1.04×10^{-2}	2.32×10^{-4}
Mg	3.62×10^{-5}	8.24×10^{-5}	6.80×10^{-4}	9.29×10^{-2}
Si	3.46×10^{-5}	1.02×10^{-4}	2.77×10^{-4}	3.59×10^{-2}
S	1.69×10^{-5}	4.91×10^{-5}	1.33×10^{-4}	1.58×10^{-2}
Ar	3.62×10^{-6}	1.92×10^{-5}	5.23×10^{-5}	1.11×10^{-3}
Ca	2.13×10^{-6}	6.08×10^{-6}	1.65×10^{-5}	2.54×10^{-5}
Fe	3.08×10^{-5}	1.22×10^{-4}	3.33×10^{-4}	5.12×10^{-4}
Ni	1.62×10^{-6}	6.43×10^{-6}	1.75×10^{-5}	2.68×10^{-5}
$\mu_{\rm A}$	1.29	4.18	11.37	17.46
μ	0.61	1.35	1.70	1.80

5. Ionization structure

In a medium with negligible external radiation, the main contribution to the ionization and recombination comes from collisions with thermal electrons. Defining the ionization fraction of ionization stage m of element Z as $X_m = n(Z_m)/n(Z)$, we can write the rate of change of X_m in a Lagrangian reference frame as

$$\frac{{\rm d}X_m}{{\rm d}t} = n_{\rm e}[-(\alpha_m + C_m)X_m + \alpha_{m+1}X_{m+1} + C_{m-1}X_{m-1}], \quad (20)$$

where C_m is the collisional ionization rate from ionization stage m to $m+1$, while α_m is the recombination coefficient from ionization stage m to $m-1$. Charge transfer, which is only important for temperatures below $\sim 10^5$ K, is ignored for the models in this paper. Charge transfer has, however, been included in a later version of the model, but was found to have no effect on the spectrum for the cases discussed in this paper. The initial state of the gas behind the shock front depends on the state of ionization in the pre-shock gas, and is discussed in more detail below. We follow each gas element as it cools and recombines after being shocked. In general, the recombination time will be longer than the cooling time, leading to non-equilibrium ionization, with highly ionized species being present at lower temperatures than in the steady state case. This is taken into account by recognizing that each position behind the shock corresponds to a specific time since the gas entered the shock. The time that has passed since a particular zone, now at position x, was shocked, is then evaluated from $t = \int_0^x v(x')^{-1}{\rm d}x'$.

Equation (20) is solved for the 13 most abundant elements: H, He, C, N, O, Ne, Mg, Si, S, Ar, Ca, Fe, and Ni. References for the collisional ionization and recombination rates are given in the Appendix.

In our models we neglect all external radiation, assuming that only shock heating is important for the ionization and emission. Since the radiation from the unshocked ejecta has a very low temperature compared to that of the shocked gas, this assumption is justified. Because we are only interested in the X-ray emitting gas, the effects of the X-rays on the cool shell can also be neglected. The reprocessing of the X-rays is, however, important (CF94) for the optical and UV radiation. In addition, the temperature is low enough, while the density is high enough, for ion and electron temperatures behind the shock to be nearly in equilibrium (FLC96). We also neglect thermal conduction between the zones. This is discussed further in Sect. 6.3.

The state of ionization immediately behind the shock is set by that of the pre-shock gas. This is in turn determined by the X-ray photoionization from the shock. A self-consistent solution of the two ionization states is therefore needed. As usual, the photoionized gas is characterized by the photoionization parameter $\zeta = L/n_{\rm e}r^2$ (e.g., Tarter et al. 1969). Using Eqs. (3) and (36) we find that

$$\zeta = 10.4\left(\frac{\mu\mu_{\rm A}}{\mu_{\rm A}-\mu}\right)\left(\frac{V_{\rm rev}}{1000\ {\rm km\,s^{-1}}}\right)^3. \quad (21)$$

For a solar composition $\zeta = 12.0(V_{\rm rev}/1000\ {\rm km\,s^{-1}})^3$, and $\zeta = 20.9(V_{\rm rev}/1000\ {\rm km\,s^{-1}})^3$ for an oxygen-dominated composition. The most important point here is that ζ only depends on the reverse shock velocity and the chemical composition, but not on e.g., the mass loss rate parameter, A_*. The pre-ionization therefore does not introduce any more parameters into the problem. With $V_{\rm rev} \sim 1000\ {\rm km\,s^{-1}}$, implying $kT \sim 1$ keV, and using the results of Tarter et al. (1969) for the ionization structure based on a free-free spectrum, we expect that carbon will mainly be in the form C V–VII, oxygen mainly O VI–VIII, and neon mainly Ne VIII–IX. This is confirmed by the models in Fransson (1984).

To calculate the pre-shock state we use the shock spectrum as input to an updated version of the photoionization code in CF94. The result of this is then used as input to the shock calculation. If necessary, the new shock spectrum resulting from

this can be used for a new calculation of the pre-shock structure, etc. In practice, this converges after the first iteration.

6. Emission

6.1. Continuum emission

We include free-free and free-bound emission, as well as two-photon decay from H-like and He-like ions. The emissivity (integrated over 4π) for the free-free and free-bound continuum is given by (Sutherland & Dopita 1993)

$$\epsilon_{\lambda\mathrm{ff,fb}} = 2.05\times10^{-19} n_\mathrm{e}^2 G_\mathrm{c} \lambda^{-2} \times \mathrm{e}^{-E/kT} T^{-1/2} \quad \mathrm{ergs\ s^{-1}\ cm^{-3}\ \AA^{-1}}, \tag{22}$$

where the total Gaunt factor G_c is the sum of the Gaunt factors for the free-free and free-bound transitions, and is written as

$$G_\mathrm{c} = G_\mathrm{ff} + G_\mathrm{fb}. \tag{23}$$

Sutherland & Dopita (1993) and Mewe et al. (1986) include a Gaunt factor for the two-photon emission as well. For this paper we evaluate the two-photon contribution explicitly from the level populations, as described below. Any quenching of this at high densities is therefore taken into account. The bound-free Gaunt factor is evaluated according to the method of Mewe et al. (1986), which we also follow for the free-free emission.

$$G_\mathrm{ff} = \frac{n_\mathrm{H}}{n_\mathrm{e}} \sum_{Z,i} A_Z X_m(Z) z_{n_0}^2 g_\mathrm{ff}. \tag{24}$$

For the individual free-free Gaunt factors, g_ff, we use the calculations of Sutherland (1998). A_Z is the abundance of element Z and z_{n_0} is the effective charge of the ground state, defined by

$$E_\mathrm{ion}^{m-1}(Z) = E_\mathrm{ion}(\mathrm{H}) \frac{z_n^2}{n^2} \tag{25}$$

where, n is the principal quantum number.

For the two-photon emission, we calculate the emissivity as

$$\epsilon_{\lambda 2\gamma} = \sum_{Z,z} n_{2\gamma}(Z,z) A_{2\gamma}(Z,z) E_0 \phi(y), \tag{26}$$

where the sum goes over H-like and He-like ions, z, of all elements Z. Further, $n_{2\gamma}$ is the density of the upper level of two-photon transitions in ion (Z,z) (either $2s^2S_{1/2}$ or $2s^1S_0$), E_0 the energy difference between the levels, and $\phi(y)$ the normalized distribution function of the total two-photon emission that comes out at energy y, with $y = E/E_0$. For H-like ions we use the distribution function of Goldman & Drake (1981), while we use data from Drake et al. (1969) for He-like ions. The total emissivity is then

$$\epsilon_\lambda = \epsilon_{\lambda\mathrm{ff,fb}} + \epsilon_{\lambda 2\gamma}. \tag{27}$$

6.2. Line emission

In a collisionally ionized, low density plasma the main processes responsible for populating the excited levels are collisional and radiative excitation and de-excitation. We can then write the rate of change of the population $n_{m,k}$ of level k of ion m as

$$\begin{aligned}\frac{\mathrm{d}n_{m,k}}{\mathrm{d}t} &= -n_{m,k} n_\mathrm{e} (\alpha_{m,k} + C_m) \\ &\quad -n_{m,k} \sum_{j<k} (A_{kj}\beta_{kj} + C_{kj} n_\mathrm{e}) \\ &\quad -n_{m,k} \sum_{j>k} C_{kj} n_\mathrm{e} + \sum_{j<k} n_{m,j} C_{jk} n_\mathrm{e} \\ &\quad + \sum_{j>k} n_{m,j} \left(A_{jk}\beta_{jk} + C_{jk} n_\mathrm{e}\right) \\ &\quad + n_{m+1}\alpha_{m+1,k} n_\mathrm{e} + n_{m-1} n_\mathrm{e} C_{m-1},\end{aligned} \tag{28}$$

where A_{jk} is the transition probability, β_{kj} the escape probability, $\alpha_{m+1,k}$ the recombination rate from ion $m+1$ to ion m, level k, and C_{m-1} the collisional ionization rate from ion $m-1$ to ion m. Then C_{kj} and C_{jk} are the rate coefficients of collisional excitation and de-excitation, respectively, with

$$C_{kj} = \frac{g_j}{g_k} C_{jk} \mathrm{e}^{-(E_j - E_k)/kT} \qquad j > k, \tag{29}$$

where g_k and g_j are the statistical weights of levels k and j, respectively.

Radiative recombination to individual levels is included for He-like, Li-like, and Na-like ions, while dielectronic recombination to individual levels is included only for Fe XVII and Fe XVIII. For the ions where radiative recombination to individual levels is included we scale the rates to the individual levels with the total recombination to the ion, which includes the dielectronic recombination, thus distributing this contribution among the levels. We find that recombination to individual levels, where it is included, has little effect on the level populations. We assume that all collisional ionization takes place to and from the ground states. Similarly, recombination from ion m to $m-1$ is assumed to only occur from the ground state, so that $\alpha_{m,k} = 0$ for $k > 0$.

In the Sobolev approximation, the escape probability is calculated from

$$\beta_{kj} = \frac{1 - \mathrm{e}^{-\tau_{kj}}}{\tau_{kj}}, \tag{30}$$

where the optical depth of the transition $k \to j$, τ_{kj}, is given by

$$\tau_{kj} = n_m \sigma_{kj} \mathcal{L}_\mathrm{s} \left(1 - \frac{g_k n_{m,j}}{g_j n_{m,k}}\right). \tag{31}$$

Here n_m is the density of ion m, σ_{kj} the cross section for the transition, given by

$$\sigma_{kj} = \frac{A_{jk} n_{m,k} \lambda_0^3}{8\pi v_\mathrm{th}} \frac{g_j}{g_k}, \tag{32}$$

and $\mathcal{L}_\mathrm{s}$ is the Sobolev length, defined as

$$\mathcal{L}_\mathrm{s} = v_\mathrm{th} \frac{\mathrm{d}r}{\mathrm{d}v}, \tag{33}$$

where v_th is the thermal velocity. The Sobolev approximation holds as long as the size of the emitting region is larger than the Sobolev length, $\mathcal{L}_\mathrm{s}$. In the opposite case we use the physical

thickness of the region instead of $\mathcal{L}_s$. As an estimate of dv/dr, we take the velocity gradient from the shock to where the temperature has fallen to half of its initial value. This approximation does not hold for low temperatures, when the velocity gradient steepens. However, the net effect is that we overestimate the absorbing length, and thus the optical depth, and since we find that even in this case optical depth effects are not important (see Sect. 7.4), the errors introduced by this method are negligible. When computing the Sobolev length for lines formed in a given shell, we use the thermal velocity in that shell.

Once the level populations have been found, the volume emissivity, ϵ_{kj}, in each line is computed according to

$$\epsilon_{kj} = n_{m,k} A_{kj} E_{kj} \beta_{kj}, \tag{34}$$

where E_{kj} is the energy difference between levels k and j.

A list of all ions for which level populations are calculated is given in Table A.1 in the Appendix, as well as references for the atomic data. The majority of the atomic data have been taken from version 4.2 of the Chianti database (Dere et al. 1997; Young et al. 2003). After this paper had been submitted, we tested the code with version 5.1 of Chianti (Landi et al. 2005), but it only gave negligible effects. To speed up the calculations, only the level populations for ions that have an appreciable abundance are calculated in each zone.

The total cooling per unit volume in Eq. (17) is calculated by adding the contributions from line emission and continuum processes

$$\sum_{\lambda} \epsilon_{\lambda} + \sum_{k,j} \epsilon_{kj} = n_e n_i \Lambda(T_e). \tag{35}$$

6.3. Conduction

As mentioned previously, we neglect thermal conduction in the cooling region. Previous studies have indicated that, while this is a reasonable approximation for cosmic abundances, a higher metallicity will increase the importance of conduction (Borkowski et al. 1989; Borkowski & Shull 1990).

The significance of conduction may be estimated from the ratio between the conduction length scale and the cooling length scale, $\alpha = L_{\rm cond}/L_{\rm cool}$ (Borkowski et al. 1989). The conduction length gives an estimate of how far heat can be conducted, while the cooling length determines the slope of the temperature gradient. Consequently, conduction dominates if the conduction length exceeds the cooling length, i.e. if $\alpha \gtrsim 1$. We estimate this parameter directly behind the shock in the solar and the oxygen-dominated models. For solar composition we find $\alpha \ll 1$, while for the oxygen model $\alpha \sim 0.02$, which justifies neglecting conduction even in this case.

This conclusion agrees with Borkowski et al. (1989) for the solar model, but not for the oxygen model. They argue that for a pure oxygen model the cooling rate, and therefore also α, is increased by a factor ~1000 partly due to the higher metallicity, but mainly due to non-equilibrium cooling. The latter is, however, an effect of the low shock velocities in their models, which means that the pre-shock gas is not fully ionized. Therefore, excitation and ionization of neutrals strongly enhance the post-shock cooling, thereby reducing the cooling length. This is not the case in our models, where the shock velocity is high enough for the pre-shock gas to be fully ionized. Instead, non-equilibrium cooling tends to lower the cooling rate compared to the equilibrium case, since high ionization stages are present at lower temperatures where they cool less efficiently. Therefore the non-equilibrium cooling lessens the importance of conduction in our models, which justifies the neglect of thermal conduction in the models discussed in this work. For high metallicities, conduction may become important for certain shock parameters, as it would be e.g., in supernova remnants where Fe-rich material is encountered (e.g., Sorokina et al. 2004). It is, however, unlikely to change our qualitative conclusions. In addition, any magnetic field that is present is likely to decrease the conductivity.

6.4. Line profiles

The main process responsible for broadening of the emission lines is the expansion of the interaction shell, which has a velocity of $V_s \sim 10^4$ km s^{-1}. In the thin shell approximation we may assume $V_s = V_{\rm ej}$. For a thin shell at radius r_s, the line profile of an optically thin line is flat out to the velocity of the shell. For lines that are optically thick, the line profile depends on the velocity gradient. For $V \propto r$, the line is flat, while for constant velocity it is parabolic (e.g., Ambartsumian 1957). A breakdown of the Sobolev approximation, as discussed above, may lead to double-peaked line profiles for the optically thick lines, as seen for the Hα line in SN 1998S (Fransson et al. 2005).

In addition, the ejecta will be optically thick to X-rays from the reverse shock, at least during the first few years. Therefore, only the emission from the approaching part of the shock will generally be observed.

Because the line profile in X-rays will usually be dominated by the instrumental profile, we use, for simplicity, a flat, box-like profile in all cases.

7. Results

7.1. Model parameters

The model described here is applicable to supernovae where the reverse shock is radiative. Progenitors of type II supernovae have mass loss rates in the range 10^{-6}–10^{-4} $M_\odot$ yr^{-1}. For a wind velocity $v_w = 10$ km s^{-1}, this gives $\tilde{A}_* \approx 0.1$–10, with type IIPs in the lower range and type IILs and type IIns having $\tilde{A}_* \gtrsim 1$. As we will discuss in Sect. 7.3, for $\eta \gtrsim 10$ the reverse shock is then radiative to at least a hundred days for solar composition and a shock velocity of $\lesssim 10^4$ km s^{-1}. For steeper density gradients, and for helium- or oxygen-rich ejecta, the radiative phase will be longer. The steady state condition for the reverse shock is, therefore, fulfilled for most type IIL and type IIn supernovae, at least for the first few hundred days.

Because of the moderate mass loss rates, type IIP supernovae are in general adiabatic, as discussed in Chevalier et al. (2005). Type Ib/c supernovae are thought to originate from Wolf-Rayet stars, which have much faster stellar winds with $\tilde{A}_* \sim 10^{-3}$. Therefore, the shock is not radiative beyond a few days or even hours, and consequently our models are

not applicable to type Ib/c supernovae, unless the density gradient is very steep. For these supernovae a better assumption is to employ an adiabatic model for the temperature and density. Inverse Compton scattering of photospheric photons by relativistic electrons may also contribute to the X-ray emission from type Ib/c supernovae (Björnsson & Fransson 2003). Also, inverse Compton scattering by thermal electrons behind the circumstellar shock may contribute under certain conditions (Sect. 7.9).

The parameters which characterize a given model are the temperature, composition, and density, immediately behind the reverse shock. Further, for a stationary shock the density is mainly important for the absolute flux, not for the spectral shape, as long as optical depth effects and collisional deexcitation are not important, which is in most cases a good approximation (Sect. 7.4). As we discuss below, departures from ionization equilibrium are only important at low temperatures and do not influence the spectrum above 100 eV. Altogether, this implies that *the shock spectrum is only sensitive to the reverse shock velocity and the composition.*

For the models discussed in this paper, we take $\tilde{A}_* = 1$, $V_4 = 1$, $s = 2$, and a time of 100 days after explosion, unless otherwise noted. In order to study the effects of different reverse shock temperatures or, alternatively, different chemical compositions, the density gradient of the ejecta is varied according to Eq. (4), as we vary either the temperature or the composition. We stress, however, that although the density behind the reverse shock varies with η, these parameters are only important for the scaling of the absolute flux.

The normalization of the spectrum is given by the fact that the total luminosity from a radiative shock is

$$\begin{aligned} L_{\rm rev} &= 4\pi R_{\rm s}^2 \frac{1}{2}\rho_{\rm ej} V_{\rm rev}^3 \\ &= 1.6\times 10^{41} \frac{(\eta-3)(\eta-4)}{(\eta-2)^3} \tilde{A}_* V_4^3 \ \ {\rm erg\ s^{-1}}, \end{aligned} \tag{36}$$

if $s = 2$. Because the velocity depends on time as $V \propto t^{-1/(\eta-2)}$, this means that the total luminosity of the reverse shock decreases slowly with time, as long as η is constant. However, for the *observed* flux this is more than compensated for by the decreasing optical depth in the cool, absorbing shell, which lets through more of the emitted radiation as the region expands (see Sect. 7.8). Note also that approximately half of the above luminosity is absorbed by the ejecta (Sects. 6.4, 7.9).

7.2. Shock structure

Radiative shocks occur in a wide range of circumstances in the interstellar medium, and have been discussed by a number of authors. The first numerical models of cooling shocks were made by Cox (1972), who considered a planar shock with a velocity of 100 km s^{-1} and applied the results to the Cygnus Loop. Later, improved models were developed by Raymond (1979), Dopita (1976, 1977), and others (see also Dopita & Sutherland 1996, and references therein). These models were intended for such diverse phenomena as old supernova remnants and narrow line emission regions in active galactic nuclei, but are in general not applicable to young supernovae. The reason for this is that for the low densities in supernova remnants the shock is not radiative above ∼200 km s^{-1}.

The effects of composition on the properties of the cooling gas in radiative shocks have been studied by Itoh (1981a,b, 1986, 1988), Borkowski et al. (1989), and Borkowski & Shull (1990). The main difference between these studies and the present one is again the lower velocity, $\lesssim$200 km s^{-1}, and density in their models, which is the reason for the somewhat differing results, e.g. as regards the role of conduction, as mentioned earlier.

The hydrodynamic evolution of fast shocks evolving in a dense medium, applicable to AGNs and young supernova remnants, was calculated by Plewa & Różyczka (1992) and Plewa (1993, 1995). While these models could indeed be applicable to supernovae if the composition is close to solar, their treatment of the cooling in a time-independent formalism makes it less applicable to the reverse shock. As we discuss below, a higher metallicity, as appropriate for the reverse shock, leads to a stronger cooling, and thereby a need for a time-dependent calculation of the ionization balance and cooling. They also treat the emission in a simplified manner by assuming collisional ionization balance and computing the emission in the cooling region from given line intensities. In contrast, we compute the emission from transitions in multi-level ions, and couple the resulting cooling to the hydrodynamics, resulting in detailed and self-consistent spectra.

An important feature of high velocity shocks is the creation of ionizing photons that ionize the pre-shock gas and the cooling, shocked gas (Sect. 5). If neutrals are present, some time is needed for the shocked gas to become ionized. As the shocked gas approaches ionization equilibrium corresponding to the post-shock temperature, the non-equilibrium ionization state creates strong line emission, which causes rapid cooling. For very fast shocks ($V_{\rm s} \gtrsim 500$ km s^{-1}), like the shocks considered in the present paper, the gas is, however, nearly fully pre-ionized (Sect. 5, Fransson 1984; CF94).

When ionization equilibrium has been reached, the gas cools slowly, with the ionization state adjusting to equilibrium at the local temperature more rapidly than the cooling occurs. This is where most of the emission occurs, because of the high temperature. When the local temperature falls below the one corresponding to the maximum of the cooling function, around 10^6 K, non-equilibrium ionization sets in. The gas cools rapidly until the temperature falls below 10^4 K, where photoionization heating balances cooling.

The gas close to the contact discontinuity has a temperature $\lesssim 10^4$ K and a density of $\sim(10^7\ {\rm K}/10^4\ {\rm K}) \sim 10^3$ times that of the post-shock gas, i.e., 10^{10}–10^{11} cm^{-3}, and absorbs a large fraction of the X-rays (Sect. 7.8). A large fraction of the optical and UV emission originates in the cold, dense shell (CF94).

For a given reverse shock velocity and composition, the post-shock temperature will be lower the steeper the ejecta density gradient is, but is typically $\sim 10^7$ K. This is close to the minimum of the cooling function, so in models with a lower temperature than $\sim 10^7$ K, a cooling instability will set in almost immediately, whereas models with a higher temperature will take longer before cooling starts; i.e., the interaction region will be thicker.

Table 2. Fitting parameters for the cooling function of Eq. (38) and the thickness parameter, D_0 of the cooling region, from Eq. (39).

Composition	A (erg cm^3 s^{-1})	B (erg cm^3 s^{-1})	α	β	D_0 (cm)
Solar	8.0×10^{-23}	2.3×10^{-24}	0.90	0.50	1.82×10^{17}
Helium zone	5.5×10^{-22}	1.5×10^{-23}	1.10	0.40	1.50×10^{18}
Carbon zone	1.9×10^{-20}	1.3×10^{-22}	1.35	0.40	1.20×10^{18}
Oxygen zone	4.5×10^{-20}	2.8×10^{-22}	1.00	0.40	4.61×10^{16}

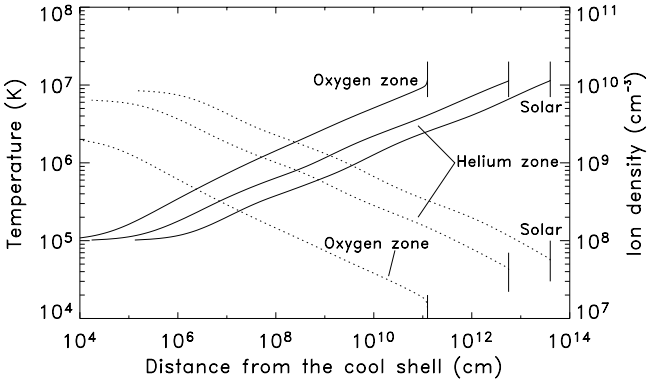

Fig. 2. Density (dashed lines) and temperature (solid lines) behind the reverse shock as a function of distance from the contact discontinuity in a model with $V_4 = 1$, $s = 2$, $\tilde{A}_* = 1$, and $T_0 = 1.0$ keV at 100 days after the explosion and for three compositions. In these models the radius of the interaction region is $R_s = 8.64 \times 10^{15}$ cm. The vertical lines indicate the position of the shock with respect to the cool shell in the three cases.

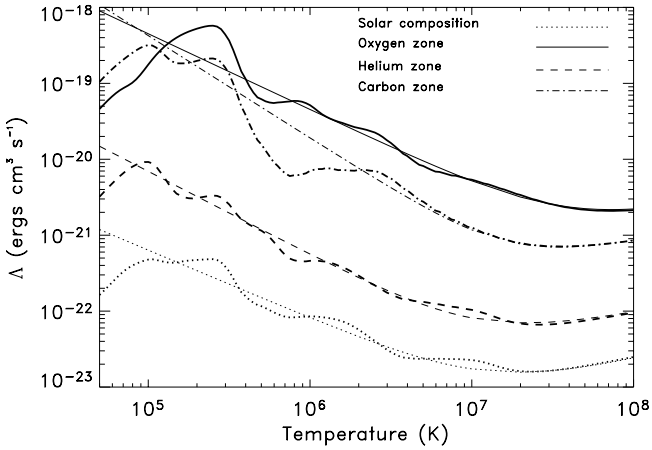

Fig. 3. Cooling curves for four compositions. Cooling functions from the model calculations for each composition, assuming ionization equilibrium, are plotted with the corresponding analytical fit, with the fitting parameters given in Table 2.

In Fig. 2 we show the density and temperature structure for our standard model with $V_4 = 1$, $\tilde{A}_* = 1$, and $T_0 = 1.0$ keV at 100 days after the explosion and for three compositions. To show the drop in temperature and ionization close to the cool shell more clearly, we plot this *as the distance from the end of the cooling instability*, rather than from the shock.

An analytical estimate of the thickness of the cooling region may be obtained from the cooling time and the velocity of the post-shock gas, $V_{\rm rev}/4$, so that $D = t_{\rm cool} V_{\rm rev}/4$ where

$$t_{\rm cool} = \frac{3kT\,(n_{\rm e} + n_{\rm i})}{2\Lambda n_{\rm e} n_{\rm i}} = \frac{3kT}{2\,(1 - \mu/\mu_{\rm A})\,n_{\rm i}\Lambda}. \tag{37}$$

The equilibrium cooling function may be fit by a function of the form

$$\Lambda = AT_6^{-\alpha} + BT_6^{\beta}, \tag{38}$$

where $T_6 = T/10^6$ K and the fitting parameters A, B, α, and β depend on the composition of the gas; see Table 2 for the compositions considered here. In the range 10^5–10^9 K, which are the temperatures contributing to the X-ray emission, the fits are in general valid to within a factor of 2. The exceptions are the carbon and oxygen models, for which the cooling below 10^6 K varies strongly. The fits to the cooling functions are plotted in Fig. 3, together with the cooling functions from our model calculations, assuming ionization equilibrium.

For the temperatures of interest, only the first term of the cooling function in Eq. (38) contributes. Combining this with Eq. (37) and using Eqs. (4) and (6) for the temperature, we can express the thickness of the region as

$$\begin{aligned} D \;&\sim\; \frac{1.45 \times 10^{-8}}{A} \frac{\mu_{\rm A}^2 \mu^{1+\alpha}}{(\mu_{\rm A} - \mu)} \\ &\quad \times \frac{\left(2.27 \times 10^3\right)^{\alpha}}{(\eta - 3)(\eta - 4)(\eta - 2)^{3+2\alpha}} \frac{t_{\rm d}^2}{\tilde{A}_*} V_4^{5+2\alpha} \\ &= \frac{D_0}{(\eta - 3)(\eta - 4)(\eta - 2)^{3+2\alpha}} \frac{t_{\rm d}^2}{\tilde{A}_*} V_4^{5+2\alpha}, \end{aligned} \tag{39}$$

where the time is in days since the explosion, and we have set $s = 2$. The composition dependent constant D_0 is given in Table 2 for the four compositions considered here.

For the model parameters above ($V_4 = 1$, $\tilde{A}_* = 1$, $T_0 = 1$ keV), the analytical estimate gives $D \sim 2.1 \times 10^{14}$ cm for solar composition, while the model calculations give $D \sim 5.3 \times 10^{13}$ cm. The factor of four difference results from the approximate form of the cooling function in Eq. (38) and from the increase in cooling as the temperature drops, leading to a collapse of the region. For the non-solar models the analytical estimates give $D \sim 3.5 \times 10^{13}$ cm for the helium model, $D \sim 2.8 \times 10^{12}$ cm for the carbon model, and $D \sim 6.7 \times 10^{11}$ cm for the oxygen model. The numerical results for these models are $D \sim 7.8 \times 10^{12}$ cm, $D \sim 9.4 \times 10^{11}$ cm, and $D \sim 3.1 \times 10^{11}$ cm, respectively. In all cases the thickness of the cooling gas is much smaller than the shock radius, justifying the thin shell and stationary approximations.

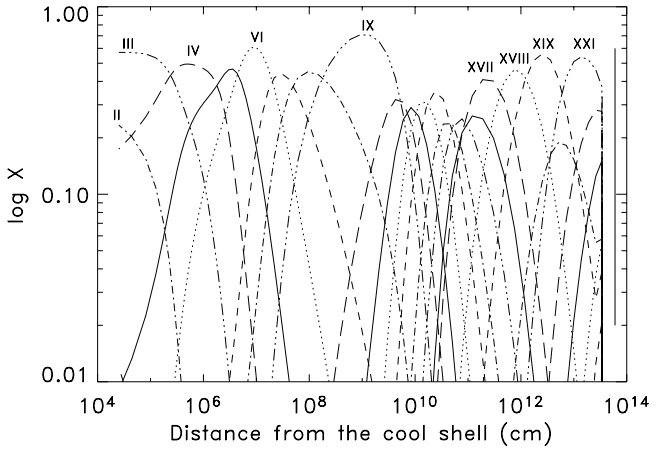

Fig. 4. Ionization structure of Fe behind the reverse shock for the solar composition model in Fig. 2. The vertical line indicates the position of the shock.

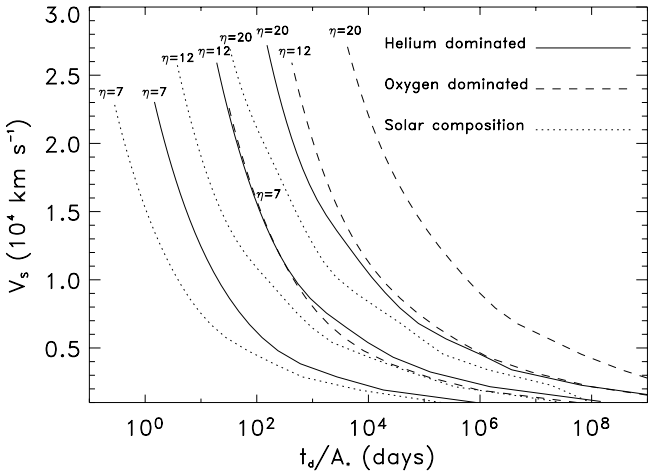

Fig. 5. Ratio of cooling time ($t_{\rm cool}$) and age ($t_{\rm d}$) of the shocked ejecta. The lines represent the limiting velocities for which the cooling time behind the reverse shock is equal to the expansion time. If the velocity of the circumstellar shock at a given time is lower than values along the curve corresponding to the relevant density slope, η, the reverse shock is radiative. If it is higher, the shock is adiabatic.

The ionization structure of Fe in the cooling region behind the reverse shock for the solar composition model is plotted in Fig. 4. We see that Fe is never fully ionized, because of the comparatively low shock temperature. Immediately behind the shock front, Fe XXI is most abundant, with noticeable fractions of Fe XVII–XXV. These ions dominate the bulk of the cooling gas, but further downstream lower ionization stages also become sufficiently abundant to affect the emission.

7.3. Cooling and ionization timescales

The main assumption of our model is that the flow behind the reverse shock is stationary, i.e., that the time needed for a process to occur is short compared to the expansion time. In this case we can calculate the temporal evolution by assuming steady state with given values of n_0 and T_0 for each epoch. For the hydrodynamic equations, the relevant timescale is the cooling timescale, given by Eq. (37).

We check the assumption of a stationary flow by estimating $t_{\rm cool}$ in all zones. Using Eq. (5) for the ion density and $s = 2$, we can express the ratio of the cooling and expansion timescales as

$$\frac{t_{\rm cool}}{t} = \frac{6.7\times10^{-22}\mu_{\rm A}^2\mu V_4^4 t_{\rm d}}{(\mu_{\rm A}-\mu)(\eta-2)^2(\eta-3)(\eta-4)\Lambda(T)\tilde{A}_*}, \quad (40)$$

where $t_{\rm d}$ is the time in days since the explosion. The cooling time is thus determined by the shock velocity, $V_{\rm s}$, and the ratio $t_{\rm d}/\tilde{A}_*$.

In Fig. 5 we plot this relation for $s = 2$, three different values of η, and three of the chemical compositions in Table 1. For a particular value of $\tilde{A}_*$ the reverse shock is radiative at a given time, $t_{\rm d}$, if the velocity of the outer shock is below the curve corresponding to the ejecta density profile. We see that the higher the value of η, the larger the range of shock velocities for which the reverse shock becomes radiative early on. The same is true as we go from solar composition to more metal-rich gas.

Due to the nearly constant pressure behind the reverse shock, $n_{\rm e} \propto T_{\rm e}^{-1}$ in the post-shock region. The density in a model with $T_0 = 10^7$ K will therefore increase by a factor $\sim10^2$ before reaching $T_{\rm e} \sim 10^5$ K. Therefore, if the assumption of stationarity holds immediately behind the reverse shock, it will be a good approximation in all of the post-shock gas.

Although it has been found that in a supernova remnant the ionization structure must be modeled by a time-dependent formalism (e.g., Kaastra & Jansen 1993; Sorokina et al. 2004), it is not clear if this is also the case for a young supernova, where the densities are much higher. We will, therefore, next explore the differences between steady state and time-dependent calculations for the ionization balance for a variety of parameters and compositions (Table 1).

For the ionization balance, the requirement is that the collisional ionization parameter $\tilde{t}_{\rm rel} = n_{\rm e}t_{\rm rel}$ be sufficiently small compared to the expansion and cooling timescales. The relaxation time for a particular ion, $t_{\rm rel}$, is the shortest of the ionization and recombination times (e.g., Mewe 1999), given by $t_{\rm ion} = [C(T_{\rm e})n_{\rm e}]^{-1}$ and $t_{\rm rec} = [\alpha(T_{\rm e})n_{\rm e}]^{-1}$, where $C(T_{\rm e})$ and $\alpha(T_{\rm e})$ are the collisional ionization and recombination coefficients, respectively, for a given ion at a specific temperature. There is, therefore, a specific, temperature-dependent relaxation parameter for each ion, which can be expressed as $\tilde{t}_{\rm rel} = \min[1/C(T_{\rm e}), 1/\alpha(T_{\rm e})]$. In Fig. 6 we show how this parameter for Fe II–XXVI varies with temperature for $T \gtrsim 10^5$ K. At high temperatures it is given by the ionization timescale, while at lower temperatures it is determined by the recombination time. The relaxation parameter depends only on atomic physics.

Let us first consider the ratio of $\tilde{t}_{\rm rel}$ to the expansion timescale, t. For a given temperature, a limiting density above which steady state applies may be found from

$$n_{\rm e}t \gtrsim \tilde{t}_{\rm rel}(T). \quad (41)$$

Using the ion density from Eq. (5), writing the electron density as $n_{\rm e} = n_{\rm ion}(\mu_{\rm A}-\mu)/\mu$, and assuming $s = 2$, this relation

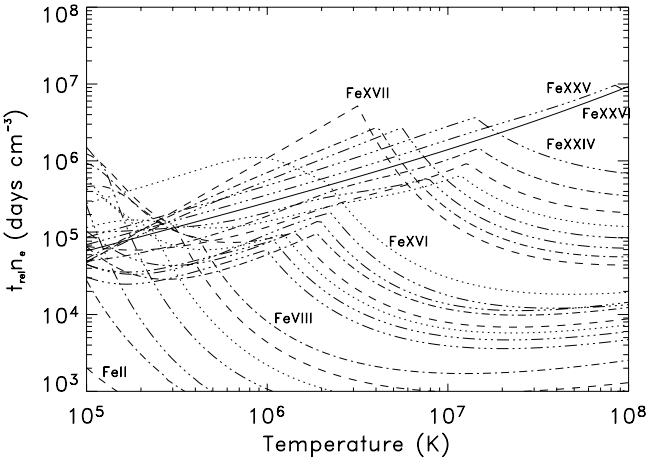

Fig. 6. The lines represent the collisional ionization parameter, $\tilde{t}_{\rm rel} = t_{\rm rel} n_{\rm e}$ for Fe, with $t_{\rm rel}$ in days.

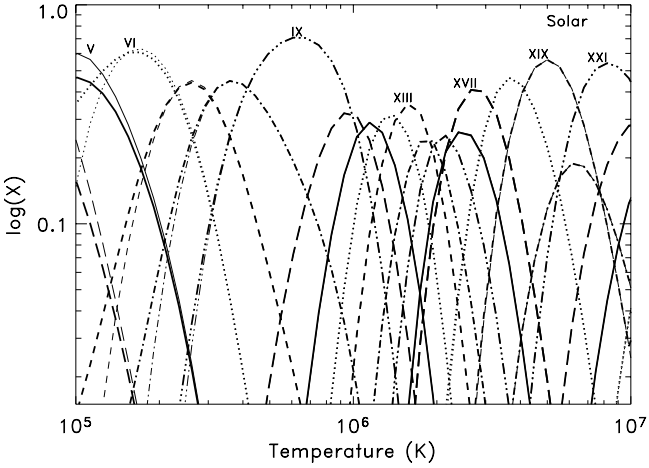

Fig. 7. Ionization structure of Fe behind the reverse shock as a function of temperature. The thin lines are the steady state model, and the thick lines are for a time-dependent ionization. The input parameters are the same as for the model in Figs. 2 and 4, and the composition is solar.

translates into the requirement that the ejecta density gradient satisfy the following relation

$$(\eta-3)(\eta-4) \gtrsim 0.12 \frac{\mu\mu_{\rm A}}{\mu_{\rm A}-\mu} \frac{V_4^2}{\tilde{A}_*} \times \left(\frac{\tilde{t}_{\rm rel}}{10^7 \text{ days cm}^{-3}}\right)\left(\frac{t_{\rm d}}{100 \text{ days}}\right). \quad (42)$$

The highest values of the relaxation parameter in Fig. 6 are those of Fe XXV and Fe XXVI at $T = 10^8$ K, where $\tilde{t}_{\rm rel} \sim 10^7$ days cm^{-3}. This is also among the highest values of $\tilde{t}_{\rm rel}$ for any ion, and can therefore be used as an upper limit to $\tilde{t}_{\rm rel}$. For the set of parameters used in this paper ($A_* = V_4 = 1$, see Sect. 7.1), we find that this relation is fulfilled for both the solar and higher metallicity models up to several hundred days for all interesting values of η. Only for shocks with very high velocity and low mass loss rate is the expansion timescale shorter than the ionization timescale.

For steady state ionization to hold, the relaxation time for ionization must also be shorter than the local cooling time, $\tilde{t}_{\rm rel} < t_{\rm cool}$. The cooling time decreases rapidly as the temperature drops in the post-shock gas, and a shock for which steady state holds at the shock front may be out of equilibrium further downstream. In terms of the collisional ionization parameter and the cooling function we get

$$\tilde{t}_{\rm rel} < \frac{3\mu k T}{\mu_{\rm A}\Lambda}. \quad (43)$$

Using the first term of the cooling function in Eq. (38), for $T_{\rm e} \lesssim 10^7$ K we can express the condition for steady state ionization as

$$\tilde{t}_{\rm rel} < \frac{4.8\times10^{-15}\mu}{\mu_{\rm A} A} T_6^{1+\alpha} \text{ days cm}^{-3}. \quad (44)$$

This requirement should be checked for each ion at the temperatures where the ion is abundant. Note that this only depends on the temperature and composition, but not on the density.

As an example we consider Fe in the solar composition model for which the collisional ionization parameter is shown in Fig. 6. Using $\tilde{t}_{\rm rel} \sim 10^7$ days cm^{-3} as an upper limit to $\tilde{t}_{\rm rel}$ as discussed above, we can determine a lower limit to the temperature, $\sim 5 \times 10^6$ K, above which steady state can be assumed to hold. Below this temperature, time-dependent effects are expected to become important, although the fact that $\tilde{t}_{\rm rel}$ varies with the temperature means that steady state will also be a reasonable approximation at somewhat lower temperatures. The corresponding requirement for the helium model is $T \gtrsim 1.8 \times 10^6$ K, while the requirement for the carbon and oxygen-dominated models is $T \gtrsim 1.1 \times 10^7$ K and $T \gtrsim 3 \times 10^7$ K, respectively.

From this we expect steady state to be a reasonable approximation for the X-ray emitting part of a solar composition and a helium-dominated shock. The carbon and oxygen-dominated shocks, on the other hand, are expected to already be out of equilibrium at the shock front. For these shocks a fully time-dependent ionization balance calculation is required, as we indeed do in this paper.

To illustrate this quantitatively, we show the ionization structure of Fe in Figs. 7 and 8, both for steady state and time-dependent ionization in our standard model with solar composition and oxygen-dominated composition, respectively. We see that in the solar case the state of ionization behind the shock follows steady state until the gas has cooled to a few times 10^5 K. After that, recombination begins to lag behind cooling, the effects being noticeable in Fe VI and lower ions, which is what we would expect from the estimate above. Since this occurs at such low temperatures, it has no noticeable effect on the X-ray emission.

For the carbon and oxygen-dominated models non-equilibrium effects are already important for Fe XXI at 7×10^6 K, as we expected. As extreme examples, we note in Fig. 8 that the concentrations of Fe XVII and Fe XVIII stay high at considerably lower temperatures than in the steady-state case, due to the long recombination time compared to the cooling time. Except for $\lambda \gtrsim 100$ Å, the effects on the spectra are, however, minimal.

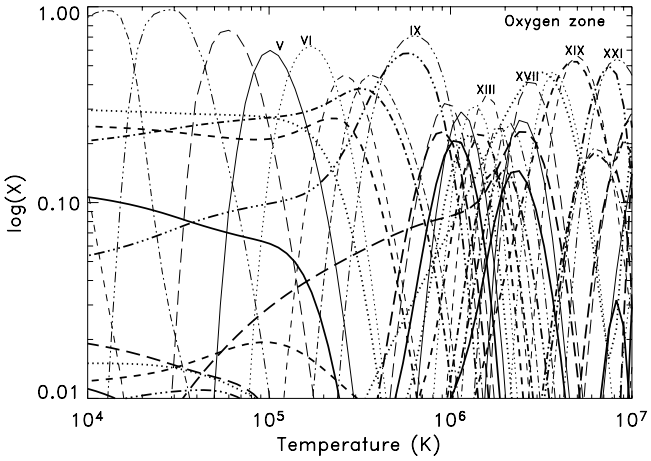

Fig. 8. The same as in Fig. 7, but for an oxygen-dominated composition.

From this discussion we conclude that the equilibrium assumption is reasonable, except for low temperature shocks, and shocked gas highly enriched in heavy elements. This is useful since it allows a very simplified calculation of the shock emission, without a fully time-dependent formalism.

7.4. Optical depth and density effects

Radiative transfer is taken into account by means of the escape probability formalism described in Sect. 6, but it turns out to have little effect. To understand the reason for this, we estimate the optical depth, τ, for typical parameters. Combining Eqs. (31) and (32) and using the total size of the region, D, instead of the Sobolev length, as is more realistic,

$$\tau \sim 4.9 \times 10^{-12} n_{\rm e} D A(Z) X_m \frac{f_{kj}}{E_{kj} T^{1/2}}, \quad (45)$$

where $A(Z)$ is the abundance of element Z, X_m the ionization fraction of ion m, and E_{kj} the energy of the transition in eV.

As particularly interesting examples, we consider two of the strongest lines, the He-like O VII λ21.60 and the H-like O VIII λ18.97 resonance lines, with $f = 0.69$ and $f = 0.27$, respectively. For collisional ionization equilibrium, the maximum abundance of O VII occurs at $T \sim 8 \times 10^5$ K, where $X_m \sim 1$, and for O VIII at $T \sim 2.5 \times 10^6$ K, where $X_m \sim 0.5$. If we now write

$$\tau = \tau_0 A(Z) N_{21}, \quad (46)$$

where N_{21} is the total column density in units of 10^{21} cm^{-2}, we find that $\tau_0 = 6.6 \times 10^3$ for O VII λ21.60 and $\tau_0 = 6.4 \times 10^2$ for O VIII λ18.97.

The column density of the cooling gas is

$$N \approx \frac{1}{4} t_{\rm cool} V_{\rm rev} n_{\rm i} = \frac{3}{8} \frac{k T_0 V_{\rm rev}}{(1 - \mu/\mu_{\rm A}) \Lambda(T_0)}, \quad (47)$$

so it only depends on the composition and reverse shock velocity, but not on the mass loss rate or shock radius. For solar composition and $T_0 \sim 10^7$ K, we get $N \sim 10^{21}$ cm^{-2}. Further, $A(\rm O) = 6.9 \times 10^{-4}$, so we obtain $\tau \sim 4.4$ for O VII λ21.60 and $\tau = 0.44$ for O VIII λ18.97.

For an oxygen-dominated composition we get $\tau \sim 5.6 \times 10^3 N_{21}$ in the same way for O VII λ21.60. Because of the stronger cooling, the radiating region is also much thinner (Sect. 7.2). Our model calculation yields a thickness of 4×10^{11} cm and a column density $N_{21} \sim 6.3 \times 10^{-3}$ for the same input parameters as above. Therefore, the higher oxygen abundance results in an optical depth of O VII that is comparable to that of the solar model. Some of the strongest lines may therefore be marginally optically thick. The great majority, however, have $\tau \lesssim 1$.

One consequence of an optical depth higher than unity is that collisional de-excitation or transfer between different L and S states may become important. The ratio of collisional de-excitation to radiative escape is given by $n_{\rm e} C_{kj}/\beta_{kj} A_{kj} \approx n_{\rm e} C_{kj} \tau_{kj}/A_{kj}$, for $\tau_{kj} \gtrsim 1$.

For the O VII resonance line the most important destruction channels are either by collisional de-excitation or by a collisional transition to the $2s\,^1S_0$ level, followed by a two-photon transition. At 10^6 K the collisional de-excitation rate is $C_{2s\,^3P_1 \rightarrow 1s\,^1S_0} = 2.4 \times 10^{-10}$ cm^3 s^{-1}, while the radiative transition rate is $A_{2s\,^3P_1 \rightarrow 1s\,^1S_0} = 3.2 \times 10^{12}$ s^{-1}. Therefore, there is a critical density, $n_{{\rm crit},2s\,^3P_1 - 1s\,^1S_0} = 2.2 \times 10^{16} N_{21}^{-1} A(\rm O)^{-1}$ cm^{-3}, above which collisional destruction dominates radiative deexcitation. The forbidden $2s\,^3S_1 \rightarrow 1s\,^1S_0$ line has $C_{2s\,^3S_1 \rightarrow 1s\,^1S_0} = 4.1 \times 10^{-11}$ cm^3 s^{-1} and $A_{2s\,^3S_1 \rightarrow 1s\,^1S_0} = 1.1 \times 10^3$ s^{-1}, and $n_{{\rm crit},2s\,^3S_1 - 1s\,^1S_0} = 2.7 \times 10^{13}$ cm^{-3}. Transitions to the singlets occur with $C_{2s\,^3S_1 \rightarrow 2s\,^1S_0} = 1.2 \times 10^{-10}$ cm^3 s^{-1}, so conversion to two-photon emission occurs at a somewhat lower density, $\sim 10^{13}$ cm^{-3}. To summarize, conversion to two-photon emission or destruction by collisional de-excitation will only be important above $\sim 10^{13}$ cm^{-3}, independent of the optical depth.

Before this occurs, collisional excitation from $2s\,^3S_1$ to $2p\,^3P_2$ will convert radiative decays in the λ22.10 $2s\,^3S_0 \rightarrow 1s\,^1S_0$ line to the λ21.80 $2p\,^3P_2 \rightarrow 1s\,^1S_0$ line, if $n \gtrsim n_{{\rm crit},2s\,^3S_1 - 2p\,^3P_2} = 7 \times 10^{10}$ cm^{-3}. Because of limited instrumental resolution, as well as velocity smearing, the individual lines will, however, be difficult to resolve. The total flux in the λ21.60–22.10 lines will therefore not be affected below $\sim 10^{13}$ cm^{-3}.

To check the dependence on the density and optical depth, we made calculations for two sets of parameters, one set with $\tilde{A}_* = 1$ at 100 days, and one set with $\tilde{A}_* = 10$ at 10 days. In both cases $\eta = 10$, $s = 2$ and $T_0 = 1$ keV. The density behind the shock is therefore a factor of 10^3 higher for the second set of parameters than in the "standard" calculations below. This range covers most cases of interest.

After adjusting by a factor of ten for the difference in mass loss rates, we find that only the He-like C V λ41.47 $2^3S_0 \rightarrow 1^1S_0$ and λ40.73 $2^3P_2 \rightarrow 1^1S_0$ lines and the corresponding O VII λ22.10 and λ21.80 lines are affected by more than 50%, as predicted from the simple arguments above. Other lines are largely unaffected by the difference in density.

We therefore expect that neither density nor optical depths should affect the fluxes appreciably, except for some He-like ions. Even in these cases the effect is likely to be hidden by the instrumental resolution or velocity broadening.

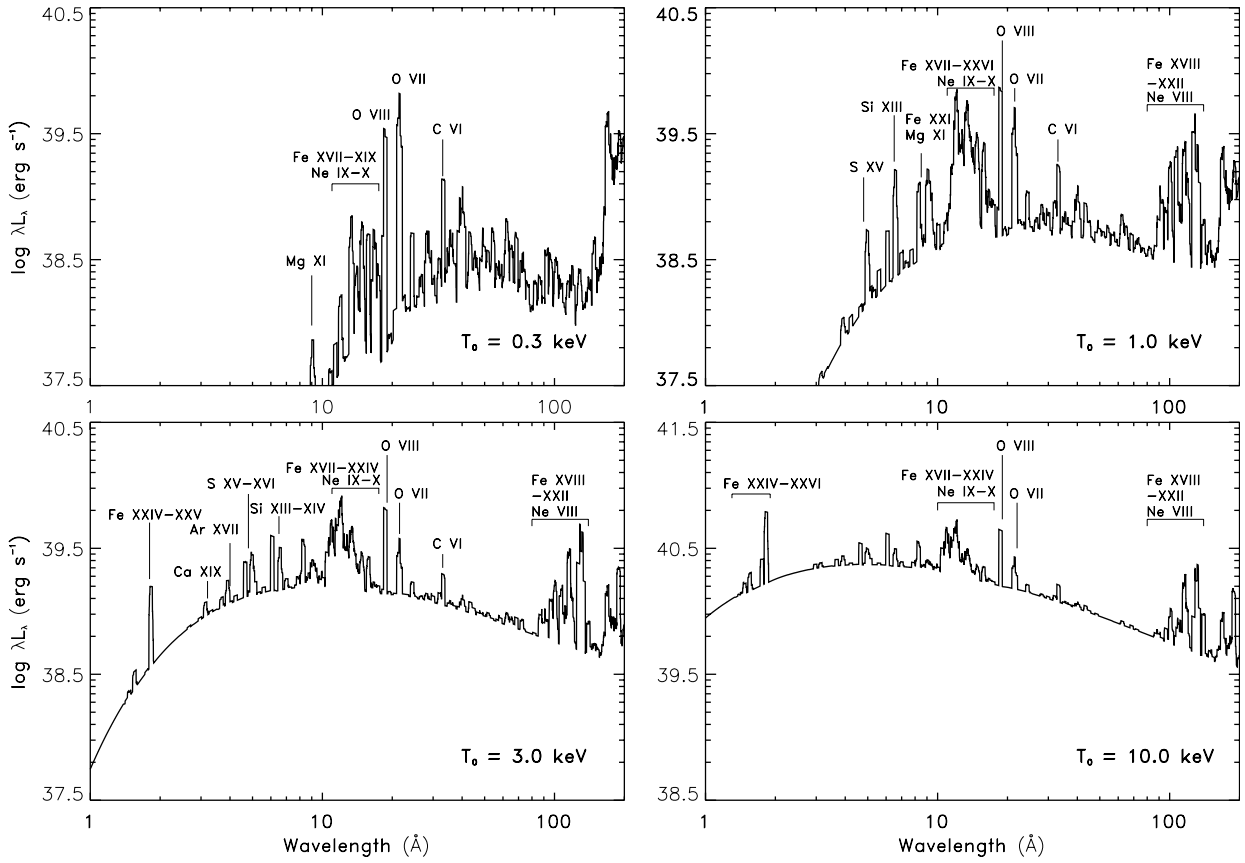

Fig. 9. Spectra with different reverse shock temperatures, T_0 = 0.3, 1.0, 3.0, and 10.0 keV, all for solar composition.

7.5. Variation with reverse shock velocity and composition

From the discussion in Sect. 7.3 we find that, as long as the steady state requirement is fulfilled, the density behind the reverse shock is of secondary importance for the spectrum, except as a normalization parameter (Eq. (36)). We therefore now discuss the effects of varying the remaining parameters, the shock temperature and the composition.

7.5.1. Reverse shock velocity

The temperature of the post-shock gas depends on the velocity of the reverse shock. In Fig. 9 we compare the spectra from four models with solar composition, where the reverse shock temperature, T_0, is 0.3 keV, 1.0 keV, 3.0 keV, and 10.0 keV. For a given shock velocity, each temperature corresponds to a particular value of the ejecta density gradient given by Eqs. (4) and (6). Here we have fixed the maximum velocity of the ejecta at $V_4 = 1$. The above reverse shock temperatures then correspond to density gradients $\eta = 22.0$ for $T_0 = 0.3$ keV, $\eta = 8.3$ for $T_0 = 3.0$ keV, and $\eta = 5.5$ for $T_0 = 10.0$ keV. The ejecta velocity is only important for the velocity broadening of the lines. To show the distribution of the flux with wavelength more clearly, we plot the luminosity per logarithmic wavelength interval, λL_λ.

The most obvious difference between the four models is the high energy exponential cutoff. Further, a higher temperature leads to a higher degree of ionization immediately behind the shock. However, because the gas is cooling, low and intermediate ionization stages are present even in the hottest model. In the models with $T_0 \gtrsim 3$ keV, the hot gas behind the shock produces little or no line emission, while contributing strongly to the continuum emission, which overwhelms the line emission from the cooler region.

Figure 10 shows the ratio of the strongest lines to the flux of the strong O VIII λ18.97 line as a function of T_0 for solar composition. The left hand panel shows the strongest lines of the metals up to Ca, while the right hand panel shows the strongest Fe lines. Note that these relative luminosities do not include the continuum contribution. It is seen from this that at low temperatures the line emission is dominated by C, N, and O, while the H- and He-like ions of Mg, Si, and S become stronger for $T_0 \gtrsim 1$ keV. Lines of especially Fe XIX, Fe XXI, Fe XXIII, Fe XXIV, and Fe XXV successively dominate the cooling for $T_0 \gtrsim 0.4$ keV.

The most conspicuous features in the $T_0 = 1$ keV and $T_0 = 3$ keV models are the Fe complexes between 10–15 Å and around 100 Å. The complex at 10–15 Å consists of emission from Fe XXI–XXIV, mixed with O VIII and Ne IX–X, while the 100 Å feature is a blend of lines from lower ionization stages of Fe, Fe XVIII–XXII, as well as O VII–VIII, Ne VIII, and Ni XXIII–XXV. These features are also present in the $T_0 = 10$ keV model, but have a smaller equivalent width due to the strong continuum. In the $T_0 = 0.3$ keV model, the Fe features are practically absent, because the high ionization stages of Fe

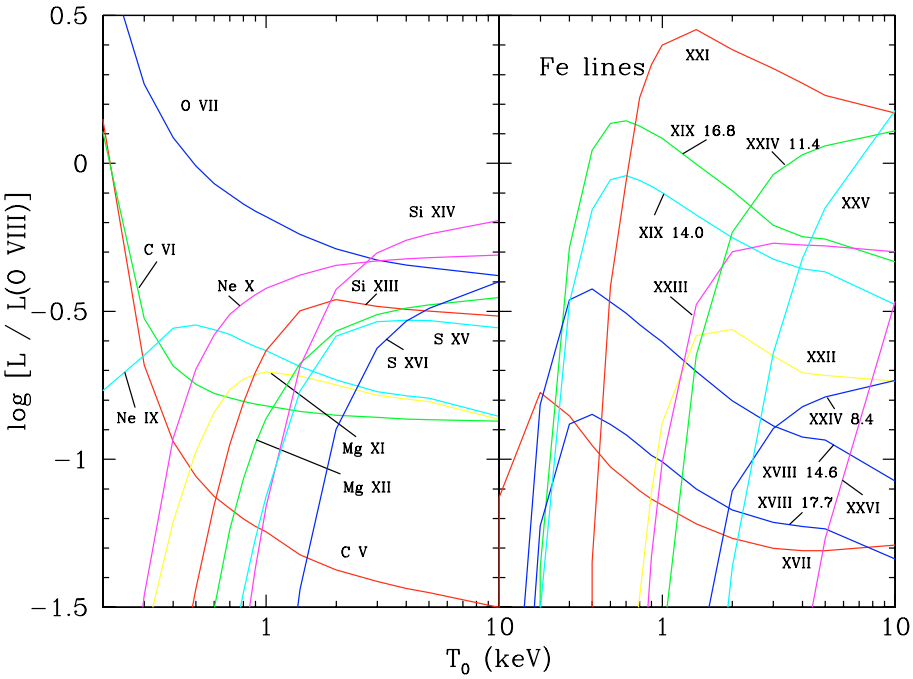

Fig. 10. Luminosities of the strongest lines relative to O VIII λ18.97 as a function of the temperature of the reverse shock. The flux-weighted wavelengths of the different labeled lines are C V λ41.5, C VI λ33.7, O VII λ22.2, Ne IX λ13.7, Ne X λ12.1, Mg XI λ9.3, Mg XII λ8.4, Si XIII λ6.7, Si XIV λ6.2, S XV λ5.1, S XVI λ4.7, Fe XVII λ17.1, Fe XVIII $\lambda\lambda$14, 6, 17.7, Fe XIX $\lambda\lambda$14.0, 16.8, Fe XX λ15.5, Fe XXI λ14.2, Fe XXII λ13.2, Fe XXIII λ12.2, Fe XXIV $\lambda\lambda$8.4, 11.4, Fe XXV λ1.87, Fe XXVI λ1.78.

are no longer present. This can be seen in Fig. 7, which shows that at a temperature of $\sim 3.5 \times 10^6$ K, Fe XVIII is the most abundant ion, while higher ionization stages of Fe are practically non-existent. Lower ionization stages of Fe have few emission lines at these energies, and the line emission in this model is therefore taken over by lighter metals.

Another line complex is seen at 175–200 Å, which mainly consists of lines from Fe X–XI, with contributions from intermediate stages of O, Ne, Ar, Ca, and Ni. This feature is strong in the $T_0 = 0.3$ keV model, but weakens with increasing shock temperature.

The emission at $\lambda \lesssim 10$ Å comes from H-like and He-like stages of Ne, Mg, Si, S, Ar, Ca, Fe, and Ni. From Fig. 10 it is apparent that these lines become increasingly stronger as the temperature increases. In the $T_0 = 3$ keV spectrum, the Fe K emission is the strongest, with the Fe XXV 1.85 Å line dominating, as well as weaker Fe XXV $\lambda\lambda$ 1.46, 1.57–1.58 lines. In the $T_0 = 10$ keV model, the Fe K lines at 1.4–1.6 Å are strong and now include Fe XXV-XXVI, as well as a contribution from Ni XXVII at 1.60 Å. In the $T_0 = 0.3$ keV model we also note the O VIII absorption edge at 17 Å, which is not seen in the other models.

7.5.2. Effects of composition

As described in Sect. 4, we calculated four models with different chemical compositions, one with solar composition, and three corresponding to the most important burning zones in the progenitor (Table 1). In Fig. 11 the spectra of the four models are shown. In all cases $T_0 = 1$ keV. As explained in Sect. 7.1, we assumed that $V_4 = 1$ in all cases, and to get the same T_0 for all compositions we have varied η. For $V_4 = 1$ a reverse shock temperature $T_0 = 1.0$ keV corresponds to $\eta = 13.0$ for the solar model, $\eta = 18.3$ for the helium-dominated model, $\eta = 20.2$ for the carbon-dominated model, and $\eta = 20.7$ for the oxygen-dominated model.

The most conspicuous features in the helium and solar models are the Fe line complexes around 10 Å and 100 Å. These features are enhanced by lines from Ne IX–X near 10 Å, and Ne VII–VIII and O VII near 100 Å; otherwise Fe dominates these features. The higher abundance of C, O, and Ne in the helium model means that these elements dominate the cooling, which can also be seen from the strength of the lines, particularly from C V–VI and Ne IX–X. Therefore, lines from heavier metals are stronger in the solar model than in the helium model, in spite of their lower abundance. This is especially apparent below 10 Å, where the line emission in both models comes from H-like and He-like Mg, Si, and S and He-like Ar, all of which are stronger in the solar model than in the helium model.

In the carbon- and oxygen-dominated models, the Fe features are more or less absent. This is because of the strong overabundance of O and Mg, as well as of Si and S, which take over the cooling in the high energy part of the spectrum. Therefore, although the Fe abundance is higher than in the other models, the Fe lines are overwhelmed by the stronger emission from lighter elements. Consequently, instead of the Fe features near 10 Å and 100 Å, the oxygen model has strong lines from a number of ions distributed over the whole spectrum, while the carbon model has few, but strong lines.

The line emission of the carbon model is dominated by lines from C V–VI, O VII–VIII, and Ne VII–X. The oxygen model, on the other hand, has only weak C emission and

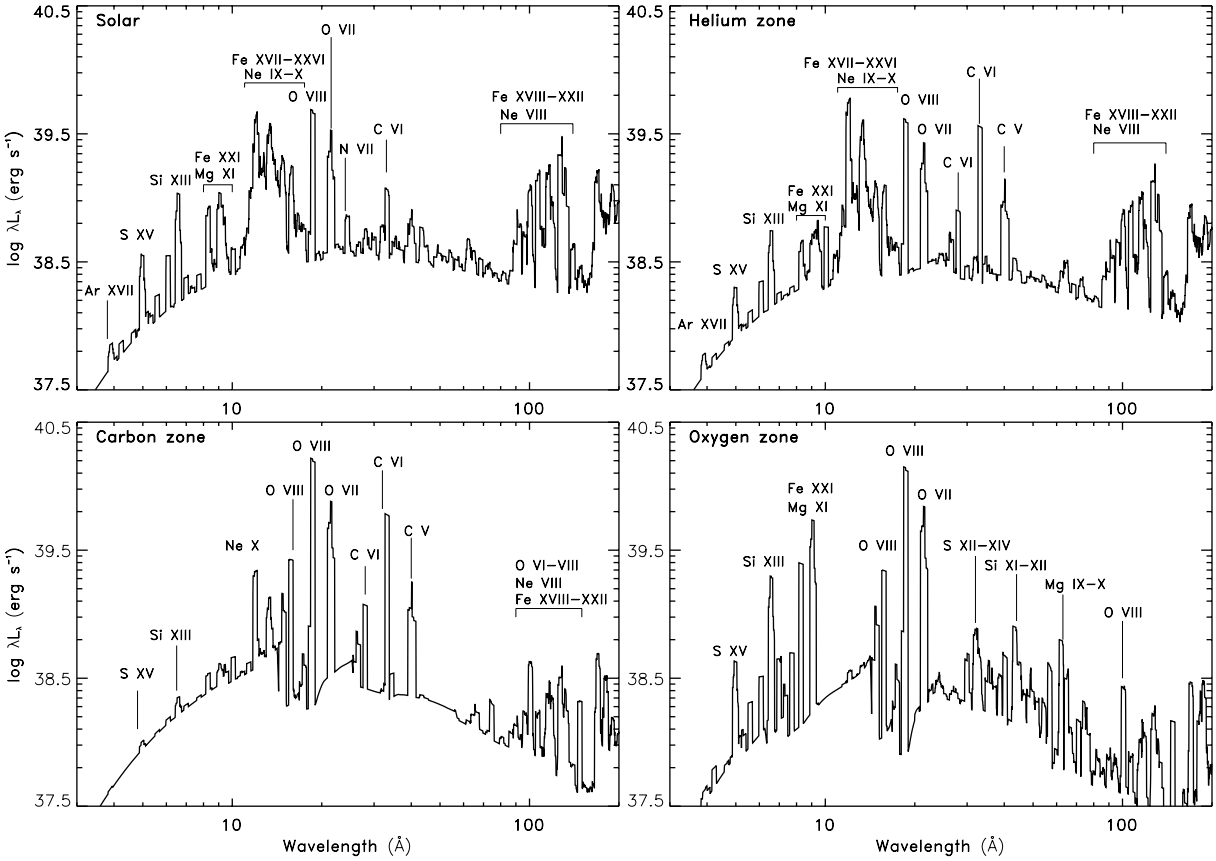

Fig. 11. X-ray spectra produced by four models with different composition. All models have $V_4 = 1$ and $T_0 = 1.0$ keV. The chemical abundances in each zone are listed in Table 1.

no Ne lines at all as a result of the low C and Ne abundances. Instead, it is dominated by emission from O VII–VIII, mixed with strong lines from H-like and He-like Mg, Si, and S, and lower ionization stages of the same elements between 10–100 Å.

The continuum of the carbon and oxygen models is considerably steeper at long wavelengths compared to the solar and helium models. This reflects the increasing importance of bound-free and two-photon contributions compared to the free-free emission in the metal-rich models. As a result both the carbon and oxygen models show strong absorption edges that are not apparent in the solar model. The most prominent is the O IX edge at 13.8 Å, which is also present, albeit weak, in the helium model. In addition, we see strong edges from Ne XI at 51.7 Å and C VII at 24.8 Å in the carbon model, and from Mg XIII at 7.3 Å and Mg XIV at 6.5 Å in the oxygen model. Also the absorption edges of Ne VIII and Si VII, which coincide at 62.0 Å, are apparent in the oxygen spectrum. In both the carbon and oxygen models, the signature of two-photon emission from O VII and O VIII is apparent, most clearly in the carbon-dominated model, where it is not obscured by line emission.

7.6. Effects of pre-ionization

As mentioned previously, the state of ionization immediately behind the shock is determined by the state of the pre-shock ejecta gas. For the 1 keV case most pre-shock oxygen is in O V–VII, while iron is found as Fe VIII–XI both for the solar and the oxygen-dominated composition. Only after $\sim\tilde{t}_{\rm rel}$ does the ionization reach the state corresponding to the local temperature.

In Fig. 12 we show the difference between the emitted spectrum when pre-ionization is included and when we assume that ionization equilibrium is reached instantly for a solar composition and for an oxygen-dominated gas. In the solar mixture the difference is barely noticeable, except for very short wavelengths, and even there it is negligible. In the oxygen-dominated gas, on the other hand, the difference is pronounced for wavelengths shorter than ∼15 Å. The reason for this is the much shorter cooling time in the oxygen-dominated model compared to the solar model. The steepening continuum emission at short wavelengths in the oxygen-dominated model is caused by the dominance of free-bound and two-photon emission over free-free emission, since both free-bound and two-photon processes are strongly affected by the lower ionization state in the post-shock gas when pre-ionization is included. For the line emission, the hydrogen-like lines are most affected by pre-ionization, as expected. We note, e.g., that the hydrogen-like Mg XII line at 8.4 Å is a factor ∼3 lower when pre-ionization is included. The helium-like Mg XI line at 9.3 Å, however, is hardly affected at all. This is as expected, since the effect of pre-ionization is to reduce the abundance of high-ionization stages close to the shock front.

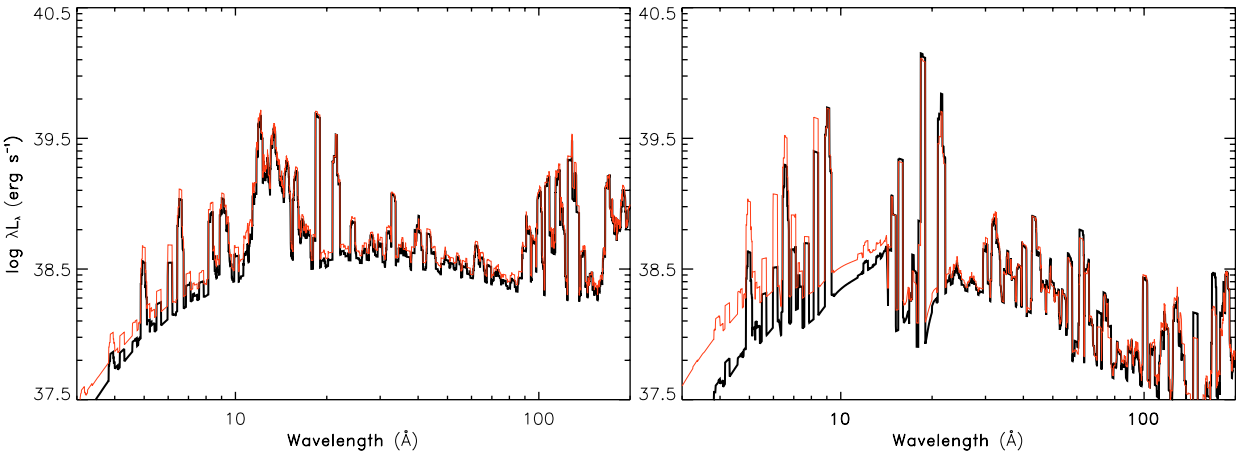

Fig. 12. Comparison between spectra where pre-ionization is included (thick line) and spectra where ionization equilibrium is assumed to be reached instantly in the post-shock gas (thin line). The left hand panel is for solar composition and the right hand panel is for an oxygen-dominated composition. In all cases $V_4 = 1$ and $T_0 = 1.0$ keV.

7.7. Comparison with single-temperature models

When X-ray observations of supernovae are analyzed, the emitting region is usually assumed to have a single temperature. In some cases two temperatures are used to account for the different temperatures of the two shocks. As an example, Uno et al. (2002) fit the ASCA observations of SN 1993J with two components, with different temperatures and absorption column densities. However, while a single temperature fit is a good approximation for the outer shock, which is adiabatic, it is far from sufficient for reproducing the emission from a radiative shock, as we will show below.

Another interesting example is the Chandra observations of SN 1993J after 8 years, which could only be fit with two low temperature components (0.35 keV and 1.01 keV) and one high temperature component (6.0 keV) (Swartz et al. 2003). Similarly Schlegel et al. (2004) find, when trying to fit spectral models to recent Chandra observations of SN 1978K, that while a two-component model gives the best fit of the models tested, the fit even for this model was not satisfactory. This indicates that more detailed models are necessary in order to fit the observed spectra. In particular, it is important to realize that the relative contribution of the different temperature components cannot be treated as free parameters, but are fixed by the hydrodynamic structure of the shock as it cools.

In Fig. 13 a spectrum produced by our combined hydro-/spectral code, with $T_0 = 1.0$ keV, is compared to a single-temperature spectrum with a temperature equal to the post-shock temperature in the whole region between the reverse shock and contact discontinuity. The spectra are normalized to have the same total luminosity between 1–10 keV. Some of the most prominent lines in each model are given in Table 3, where the fluxes relative to one of the most prominent lines in the spectra, O VIII λ 18.97, are listed for these two models, as well as for a single temperature model with $T = 0.7$ keV.

As expected, the continuum emission in the cooling model is higher at low energies, and there are more lines from lower ionization stages than in the single-temperature model. In particular, we see that the line complexes around 10 Å and 100 Å are broader in the full model than in the single-temperature model, a result of the wider range of ionization stages contributing to these features. At energies below 10 Å, the line emission in both models is dominated by H-like and He-like Mg, Si, and S, the H-like lines being stronger in the single-temperature model than in the full model. At wavelengths longer than ∼15 Å the line emission is stronger in the full model than in the single-temperature model, due to the presence of colder gas. The lines in the single-temperature model mainly come from Fe XX–XXIV, together with weaker lines from C VI, O VIII, and Ne X, while the high temperature does not allow lower ionization stages. In the cooling model the same lines are present, but also lines of lower ionization stages like C V, N VII, and O VII, as well as Si IX–XIII, S XI–XIV, Ar XIV–XVI, Ca XV–XVIII, and Fe XV–XVI.

Quantitatively, the difference can be seen from Table 3. The line ratios of, e.g., the H-like lines of the different elements differ by large factors between the two models. In reality one would not use the temperature behind the shock for a single-temperature model, but instead try to find the temperature that gives the best fit to the observed spectrum. Because of the contributions from cooler zones, the best-fit spectrum will correspond to a lower temperature than the shock temperature. When attempting to fit the shock model with $T_0 = 1.0$ keV shown in Fig. 13 with a single-temperature model, we find the best overall fit to be a single-temperature model with $T = 0.7$ keV. Although there is a slight improvement compared to the single-temperature $T = 1$ keV model, the line ratios differ by at least a factor of two from the shock model. In addition, the "best-fit" temperature is too low. To reproduce the line emission from both high and low ionization stages, a combination of cold and hot gas is therefore necessary. Note, however, that a multi-component model is not sufficient, because *the contributions from each of these components have to be calculated self-consistently, as in the shock model.* The large differences between these models are of obvious importance when determining abundances, and a too simplified analysis can lead to large errors in the results.

Table 3. Line strengths relative to the O VIII λ18.97 line for a shock model with $T_0 = 1.0$ keV, a single temperature model at the same temperature, and a single temperature model at the temperature, 0.7 keV, which gives the best fit to the spectrum of the shock model.

Ion	Wavelength (Å)	F/F(O VIII) Shock model	F/F(O VIII) Single temperature (1 keV)	F/F(O VIII) Single temperature (0.7 keV)
C VI	33.73	0.15	0.10	0.10
N VII	24.78	0.07	0.05	0.05
O VII	21.60	0.23	0.02	0.03
Ne X	12.13	0.38	0.72	0.65
Mg XII	8.42	0.14	0.60	0.29
Si XIII	6.67	0.16	0.65	0.34
S XV	5.00	0.05	0.35	0.09
Fe XXI	12.29	0.46	1.60	1.15

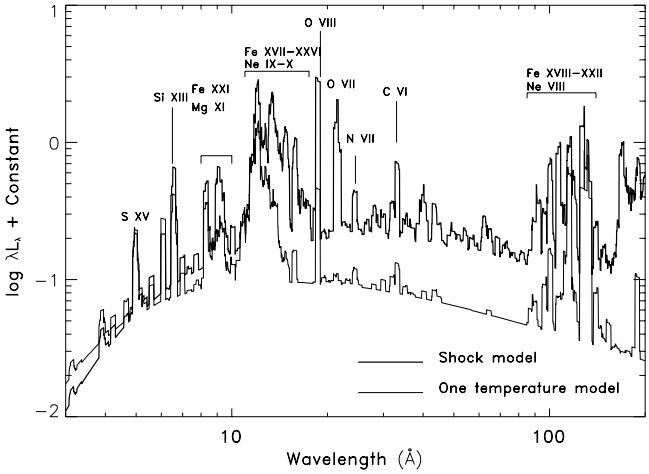

Fig. 13. Comparison between a single temperature spectrum with $T = 1.0$ keV (thin line) and a cooling shock spectrum created by our model, with $T_0 = 1.0$ keV (thick line), both with solar composition. The spectra are normalized to have the same total flux in the range 1–10 keV.

7.8. Absorption by the cool shell

When the reverse shock is radiative, most of the emission from the reverse shock is absorbed by the cool shell close to the contact discontinuity. At early epochs, only the most energetic emission passes through, while lower energies are completely absorbed. As the emitting region expands, the column density in the cool shell drops, and the shell becomes transparent, first at high energies and later at lower energies. The absorption can be taken into account by calculating the emerging luminosity at wavelength λ as

$$L_\lambda = L_{\lambda,\mathrm{em}} \mathrm{e}^{-\tau(\lambda)}, \tag{48}$$

where the subscript "em" refers to the emitted luminosity, $\tau = N_{\mathrm{col}}\sigma(\lambda)$, and $\sigma(\lambda)$ is the absorption cross section at wavelength λ, given by

$$\sigma(\lambda) = \sum_{m,Z} X_m A(Z) \sigma_{m,Z}(\lambda). \tag{49}$$

This obviously depends on the composition, but is relatively insensitive to the state of ionization of the cool shell, as long as K-shell opacity dominates. For solar composition $\sigma(\lambda) \approx 2.2 \times 10^{-25}\lambda^{8/3}$ cm^2 (CF94), where the wavelength λ is given in Å. The column density of cool gas along the line of sight depends on the swept-up mass behind the reverse shock according to Eqs. (7) and (8), so that

$$\begin{aligned} N_{\mathrm{cool}} &\approx \frac{M_0}{4\pi R^2 \mu m_{\mathrm{u}}} = \frac{(\eta-4)}{8\pi}\frac{\dot{M}}{v_{\mathrm{w}}\mu_{\mathrm{A}} m_{\mathrm{u}}}\frac{1}{r} \\ &= 1.8\times 10^{23}\frac{(\eta-4)}{\mu_{\mathrm{A}}}\tilde{A}_* V_4^{-1} t_{\mathrm{d}}^{-1}. \end{aligned} \tag{50}$$

Clumping of the cool, dense shell may, however, influence the column density (Chevalier & Blondin 1995). From their hydrodynamic calculations, Chevalier & Blondin find a variation in N_{cool} by a factor ~10 in different directions. The total emission will then be a superposition of emission along lines of sight with different column densities. Since we generally do not know the degree of clumpiness, we choose here to treat the column density as a free parameter, adjusting the absorption to fit the observations. For illustrative purposes, in Fig. 14 we show the effects of absorption using three different values for the column density, 10^{21}–10^{23} cm^{-2}. It is obvious that the low energy cutoff is very sensitive to this parameter, and for a detailed modeling a superposition of several absorption components, as given by the hydrodynamic calculations, may be needed.

7.9. X-rays from the circumstellar shock

While this paper mainly concerns a detailed modeling of the X-rays from the reverse shock, there is also a contribution from the outer, circumstellar shock. Because of the high velocity and, consequently, high shock temperature, the emission from this will be dominated by continuum emission. This has been discussed in detail in FLC96. A complication here is that the coupling between electrons and protons by Coulomb collisions decreases with increasing temperature,

$$\begin{aligned} t_{\mathrm{e-i}} &\approx 29\left(\frac{T_{\mathrm{e}}}{10^9\ \mathrm{K}}\right)^{3/2}\left(\frac{n_{\mathrm{e}}}{10^8\ \mathrm{cm}^{-3}}\right)^{-1} \\ &\approx 0.21\left(\frac{T_{\mathrm{e}}}{10^9\ \mathrm{K}}\right)^{3/2}\tilde{A}_*^{\ -1} V_4^2 t_{\mathrm{d}}^2\ \mathrm{days}. \end{aligned} \tag{51}$$

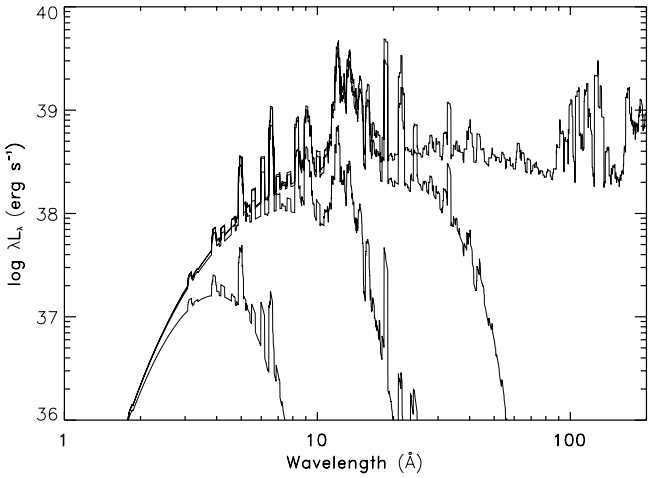

Fig. 14. The uppermost spectrum shows the energy emitted by the reverse shock for the same model as in Fig. 13, while the lower three lines represent the emerging luminosity after absorption with column densities of $N_{\rm cool} = 10^{21}$ cm^{-2}, 10^{22} cm^{-2}, and 10^{23} cm^{-2}, respectively.

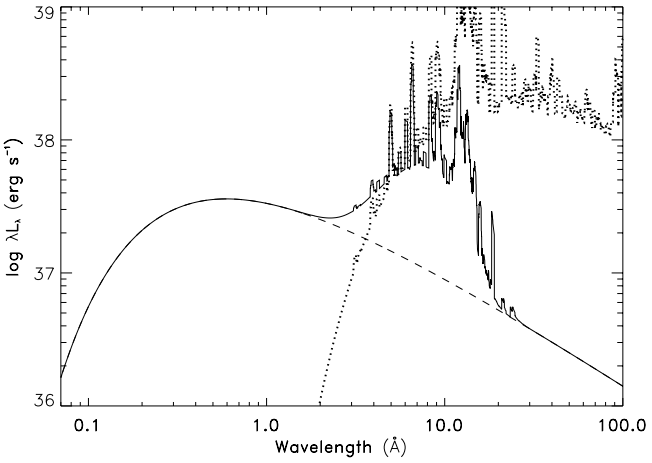

Fig. 15. Total spectrum for $V_4 = 1$, $\tilde{A}_* = 1$, $\eta = 13.0$, $T_0 = 1$ keV, $t = 100$ days, and solar composition. The solid line is the sum of the emission from the circumstellar and reverse shocks, assuming an absorbing column density of $N_{\rm cool} = 10^{22}$ cm^{-2} in the cool shell. The dotted line is the unabsorbed contribution from the reverse shock, and the dashed line is the contribution from the circumstellar shock.

The electron temperature may, therefore, be considerably lower than the ion temperature. In FLC96 it was found that, for the parameters of SN 1993J with a shock velocity of $\sim 2 \times 10^4$ km s^{-1} and $\tilde{A}_* = 5$, the ion temperature was $(1-2) \times 10^{10}$ K, while the electron temperature was only $\sim 1 \times 10^9$ K at 10 days. As the density is decreasing with decreasing $\tilde{A}_*$ and increasing time, the difference between the ion and electron temperatures can be even larger. A caveat here is, however, that plasma instabilities may lead to more efficient equipartition. The observations of SN 1993J, however, indicated that this was not very important (FLC96). For the reverse shock the density is so high and the temperature so low that the electrons and ions will generally be in equipartition.

The spectrum and luminosity of the circumstellar shock depend on the mass loss rate, $\tilde{A}_*$, shock velocity, $V_{\rm s}$, and the time since the explosion, t. In contrast to the reverse shock, the circumstellar shock is in general adiabatic. The temperature behind the shock is therefore fairly uniform (see e.g., Fig. 5 in FLC96). To estimate the monochromatic luminosity in the X-ray band we use a similar method to the one in 1996, with $s = 2$. Approximating the free-free Gaunt factor, $g_{\rm ff}$, (including relativistic effects and both ion-electron and electron-electron emission) with $g_{\rm ff} \approx 2.3 T_9^{0.42} \lambda^{0.23}$ for $1 \lesssim \lambda \lesssim 10$ Å, we get

$$L_{\lambda,\rm cs} \approx 9.6 \times 10^{37} \zeta \tilde{A}_*^2 V_4^{-1} \left(\frac{f}{0.2}\right)^{-1} \times T_9^{-0.08} \lambda^{-1.77} {\rm e}^{-0.144/\lambda T_9} \times \left(\frac{t}{100\ {\rm days}}\right)^{-1} \ {\rm erg\ s^{-1}\ \AA^{-1}}. \quad (52)$$

Here $T_9 = T_{\rm e}/10^9$ K, λ is in Å, $\zeta = [1 + 2n({\rm He})/n({\rm H})]/[1 + 4n({\rm He})/n({\rm H})]$, and f is the relative thickness of the circumstellar shock region, $f = (R_{\rm cs} - R_{\rm s})/R_{\rm s}$. For $\eta = 7$ we have $f \approx 0.3$, and for $\eta \gtrsim 12$, $f \approx 0.22$ (CF94). The luminosity from Eq. (52) should be added to the flux from the reverse shock, reduced by the factor below, in Eq. (53).

The ejecta are in general optically thick, and they absorb the emission from that part of the interaction region that is occulted by the ejecta. For the reverse shock, where the cooling region is thin, the difference in radius is so small that we can approximate the observed luminosity as one half of the emitted luminosity. This has been taken into account when plotting the model spectra. For the outer shock, on the other hand, the size of the shocked region can be as much as 20–30% of the total radius, so this approximation is inaccurate. The relation between the observed and emitted luminosity can then be expressed as

$$\frac{L_{\lambda,\rm obs}}{L_{\lambda,\rm em}} = 0.5 + 0.5 \frac{\left((f+1)^2 - 1\right)^{3/2}}{(f+1)^3 - 1}. \quad (53)$$

For $f = 0.25$ this gives $L_{\rm obs} = 0.72 L_{\rm em}$. Thus, in Fig. 15 we have reduced the outer shock emission by this factor, while the reverse shock emission has been reduced by one half, as in all other spectra.

In addition to the free-free emission, inverse Compton scattering of the photospheric photons by the thermal, semi-relativistic electrons behind the circumstellar shock may contribute to the X-ray emission (Fransson 1982; Lundqvist & Fransson 1988, FLC96). The flux of this depends sensitively on the temperature of the electrons, the mass loss rate, and the optical and UV flux of the supernova. In general, this component is only important for electron temperatures $\gtrsim 10^9$ K, and during the first months after explosion, and then only for high mass loss rates. This was discussed in some detail for SN 1993J (FLC96), where it was concluded that because of the slow equipartition between electrons and ions, the electron temperature was too low to scatter the photospheric photons up to the X-ray regime. A characteristic signature of a Compton component would be a powerlaw component to the X-rays.

The inverse Compton emission from relativistic electrons, which is responsible for the radio emission, may contribute to

the X-rays. This component is, however, only likely to be important for low values of $\tilde{A}_*$ (Chevalier et al. 2005).

As an example we show a full spectrum in Fig. 15 including the thermal emission from both shocks and the absorption by the shell for $\tilde{A}_* = 1$, $T_0 = 1$ keV, $V_4 = 1$, $\eta = 13.0$, and $N_{\rm cool} = 10^{22}$ cm^{-2} at 100 days. At this epoch the ion temperature behind the circumstellar shock is $\sim 2 \times 10^9$ K, but the electron temperature is only $\sim(1{-}4) \times 10^8$ K, due to the inefficient Coulomb coupling at the low density, $\sim 2 \times 10^6$ cm^{-3}, behind the circumstellar shock. The cutoff in the hard spectrum is, therefore, at ~0.4 Å or ~30 keV.

For $\lambda \lesssim 3$ Å ($E \gtrsim 3$ keV), the spectrum is dominated by the circumstellar shock. This is also the case above the cutoff wavelength from the cool, dense shell at ~20 Å. The figure illustrates the importance of taking both the absorption of the cool, dense shell and the circumstellar component into account when analyzing the spectrum. Note also that the column density of the cool shell is quite uncertain (Sect. 7.8). In addition, absorption from the interstellar medium, and possibly also from the circumstellar medium, should be included.

8. Conclusions

This paper discusses for the first time a detailed, self-consistent model for the X-ray emission from supernovae interacting with a dense circumstellar medium. The model that we have presented here is intended to fill a gap in the modeling of these supernovae, and is applicable to the case where the reverse shock is radiative. Our model differs from earlier models in that the spectral code is coupled to a hydrodynamical code, and that we solve the full multi-level statistical equations of each ion to calculate the line emission. The cooling and ionization, which are computed for each temperature and density, are used in the hydrodynamical equations to determine the size of the emitting region. Thus the total emission from each zone is determined self-consistently, giving the correct weight to the emission from each zone.

We have shown that for a sufficiently steep ejecta density gradient, the radiative model can be applicable up to several years, depending on the progenitor's mass-loss rate. We also show that its applicability strongly depends on the composition of the cooling gas and that the high metallicity shocks stay radiative much longer than a shock with a solar composition.

A stationary shock has been found to be a good approximation for the cases of interest to us, while the ionization must be considered in a time-dependent formulation to account for the non-equilibrium recombination in the cooling gas. This effect is, however, mainly important for lines with $\lambda \gtrsim 100$ Å. We show that the emerging spectrum is highly sensitive to both the temperature of the reverse shock and the composition of the gas. Because of the strong dependence of the emerging spectrum on the composition of the gas, the chemical abundances in the ejecta can be determined from the spectrum. A requirement for this is, however, a self-consistent modeling of the hydrodynamic and radiative processes, as demonstrated in this paper.

Acknowledgements. We are grateful to Roger Chevalier and Peter Lundqvist for comments and a careful reading of the manuscript, and to Ken Nomoto for discussions. This work was supported in part by the Swedish Research Council and the Swedish National Space Board.

Appendix A: Atomic data

The elements included in the model are H, He, C, N, O, Ne, Mg, Si, S, Ar, Ca, Fe, and Ni. Table A.1 lists the ions for which level population calculations are performed, along with the number of levels included for each ion.

The ionization rates (collisional and autoionization) are computed according to Arnaud & Rothenflug (1985), except for Fe, where we use the method suggested by Arnaud & Raymond (1992).

The recombination rates are evaluated as the sum of the radiative and dielectronic recombination coefficients, $\alpha = \alpha_{\rm r} + \alpha_{\rm d}$. For the radiative recombination rates of C, N, and O we use the fits tabulated by Nahar (1996, 1999) and Nahar & Pradhan (1997), except for C-like N and O (see below). For C-like, O-like, F-like, and Ne-like ions the recombination rates are evaluated from the fitting parameters of Zatsarinny et al. (2003, 2004a,b), using the fitting formula suggested by Verner & Ferland (1996):

$$\alpha_r(T) = a\Big[(T/T_0)^{1/2} \left(1 + (T/T_0)^{1/2}\right)^{1-b} \times \left(1 + (T/T1)^{1/2}\right)^{1+b} \Big]^{-1}. \quad \text{(A.1)}$$

The same formula is used for H-like through Ne-like ions of Mg, Si, S, Ar, Ca, Fe, and Ni (Gu 2003) and for H-like, He-like, Li-like, and Na-like ions of the remaining elements (Verner & Ferland 1996). For all remaining ions we use the rates compiled by D. Verner[2], which include data from Aldrovandi & Pequignot (1973), Shull & Van Steenberg (1982), Arnaud & Raymond (1992), Landini & Monsignori Fossi (1990, 1991), Pequignot et al. (1991), and Verner & Ferland (1996).

The dielectronic recombination rates are fitted with

$$\alpha_{\rm d}(T) = \frac{1}{T^{3/2}} \sum_{i=1}^{4} c_i {\rm e}^{-E_i/kT}. \quad \text{(A.2)}$$

For C-like, O-like, F-like, and Ne-like ions we use the fitting parameters of Zatsarinny et al. (2003, 2004a,b)[3], and for the remaining ions we use the data from Mazzotta et al. (1998).

The collisional and radiative rates for the excited levels are taken from version 4.2 of the Chianti database (Dere et al. 1997; Young et al. 2003)[4], except for the recombination to individual levels. We include radiative recombination to He-like, Li-like, and Na-like ions, using data from Verner & Ferland (1996), and dielectronic recombination to Fe XVI and Fe XVII, with data from Dasgupta (1995).

[2] Recombination rates are available from
http://www.pa.uky.edu/~verner/fortran.html

[3] Dielectronic recombination rates are available from
http://homepages.wmich.edu/~gorczyca/drdata/

[4] CHIANTI is a collaborative project involving the NRL (USA), RAL (UK), and the Universities of Florence (Italy) and Cambridge (UK).

Table A.1. Number of levels and transitions included in the model for each ion.

Ion	Lev./Trans.	Ion	Lev./Trans.	Ion	Lev./Trans.	Ion	Lev./Trans.
H I	25/75	Mg V	10/25	S XIV	40/117	Fe X	172/3959
He I	16/187	Mg VI	23/142	S XV	49/166	Fe XI	47/168
He II	25/68	Mg VII	46/389	S XVI	25/68	Fe XII	41/696
C II	18/40	Mg VIII	125/654	Ar IV	30/165	Fe XIII	27/87
C III	20/53	Mg IX	46/313	Ar VII	16/35	Fe XIV	40/227
C IV	15/18	Mg X	40/123	Ar VIII	21/34	Fe XV	53/935
C V	49/165	Mg XI	49/166	Ar IX	89/1175	Fe XVI	21/34
C VI	25/68	Mg XII	25/68	Ar X	3/3	Fe XVII	89/463
N I	26/72	Si II	15/30	Ar XI	10/24	Fe XVIII	113/176
N II	23/86	Si III	20/67	Ar XII	72/1776	Fe XIX	92/1276
N III	20/56	Si IV	21/34	Ar XIII	15/44	Fe XX	86/1309
N IV	20/59	Si V	27/115	Ar XIV	125/654	Fe XXI	290/6435
N V	15/18	Si VI	3/3	Ar XV	46/136	Fe XXII	204/6820
N VI	49/173	Si VII	10/25	Ar XVI	40/139	Fe XXIII	58/258
N VII	25/68	Si VIII	72/2061	Ar XVII	49/166	Fe XXIV	40/155
O II	15/48	Si IX	46/403	Ar XVIII	25/68	Fe XXV	49/168
O III	46/335	Si X	125/654	Ca IX	16/35	Fe XXVI	25/68
O IV	125/654	Si XI	46/134	Ca X	21/34	Ni XII	31/101
O V	20/57	Si XII	40/134	Ca XI	89/971	Ni XIII	48/191
O VI	40/107	Si XIII	49/166	Ca XII	3/3	Ni XV	27/87
O VII	49/173	Si XIV	25/68	Ca XIII	20/63	Ni XVI	40/246
O VIII	25/68	S II	43/284	Ca XIV	15/96	Ni XVII	16/35
Ne II	3/3	S III	49/366	Ca XV	46/421	Ni XVIII	21/34
Ne III	58/1212	S IV	52/220	Ca XVI	125/632	Ni XIX	89/336
Ne IV	22/91	S V	16/35	Ca XVII	46/136	Ni XX	113/176
Ne V	49/408	S VI	21/34	Ca XVIII	40/136	Ni XXI	58/1265
Ne VI	125/550	S VII	27/111	Ca XIX	49/166	Ni XXII	15/96
Ne VII	46/127	S VIII	3/3	Ca XX	25/68	Ni XXIII	20/79
Ne VIII	40/103	S IX	86/2640	Fe II	142/1268	Ni XXIV	125/654
Ne IX	49/173	S X	22/215	Fe VI	80/2083	Ni XXV	46/136
Ne X	25/68	S XI	46/416	Fe VII	9/23	Ni XXVI	40/161
Mg II	21/34	S XII	125/654	Fe VIII	83/267	Ni XXVII	49/168
Mg IV	3/3	S XIII	46/136	Fe IX	13/45	Ni XXVIII	25/68

References

Aldrovandi, S. M. V., & Pequignot, D. 1973, A&A, 25, 137
Ambartsumian, V. A. 1957, Teoretische Astrophysik, Deutscher Verlag der Wissenschaften
Arnaud, M., & Raymond, J. 1992, ApJ, 398, 394
Arnaud, M., & Rothenflug, R. 1985, A&AS, 60, 425
Borkowski, K. J., & Shull, J. M. 1990, ApJ, 348, 169
Borkowski, K. J., Shull, J. M., & McKee, C. F. 1989, ApJ, 336, 979
Canizares, C. R., Kriss, G. A., & Feigelson, E. D. 1982, ApJ, 253, L17
Chandra, P., Ray, A., Schlegel, E. M., Sutaria, F. K., & Pietsch, W. 2005, ApJ, 629, 933
Chevalier, R. 1982, ApJ, 258, 790
Chevalier, R. 1982, ApJ, 259, 302
Chevalier, R., & Fransson, C. 1994, ApJ, 420, 268 (CF94)
Chevalier, R., & Li, Z.-Y. 1999, ApJ, 520, L29
Chevalier, R., & Fransson, C. 2003, in Supernovae and Gamma-Ray Bursters, Lecture notes in physics, ed. K. W. Weiler (Springer), 598, 171
Chevalier, R., Fransson, C., & Nymark, T. 2005, in prep.
Chevalier, R. A., & Kirshner, R. P. 1979, ApJ, 233, 154
Chevalier, R. A., & Imamura, J. N. 1982, ApJ, 261, 543
Chevalier, R. A., & Blondin, J. M. 1995, ApJ, 444, 312
Chevalier, R. A., & Oishi, J. 2003, ApJ, 593, L23
Chugai, N. N. 1993, ApJ, 414, L101
Cox, D. P. 1972, ApJ, 178, 159
Dasgupta, A. 1995, ApJS, 101, 401
Dere, K. P., Landi, E., Mason, H. E., Monsignori Fossi, B. C., & Young, P. R. 1997, A&AS, 125, 149
Dopita, M. 1976, ApJ, 209, 395
Dopita, M. 1977, ApJS, 33, 437
Dopita, M., & Ryder, S. 1990, IAU Circ., 4950
Dopita, M., & Sutherland, R. S. 1996, ApJ, 102, 161
Drake, G. W. F., Victor, G. A., & Dalgarno, A. 1969, Phys. Rev. A, 180, 25
Fesen, R. A., Hammel, M. C., Morse, J., et al. 2006, ApJ, 636, 859
Filippenko, A. V. 1997, ARA&A, 35, 309
Fransson, C. 1982, A&A, 111, 140

Fransson, C. 1984, A&A, 133, 264
Fransson, C., & Björnsson, C.-I. 2005, in Supernovae, ed. J. M. Marcaide, & K. W. Weiler (Springer), IAU Coll., 192, 77
Fransson, C., Lundqvist, P., & Chevalier, R. 1996, ApJ, 461, 993 (FLC96)
Fransson, C., Chevalier, R. A., Filippenko, A. V., et al. 2002, ApJ, 572, 350
Fransson, C., Challis, P. M., Chevalier, R. A., et al. 2005, ApJ, in press
Fox, D. W., Lewin, W. H. G., Fabian, A., et al. 2000, MNRAS, 319, 1154
Goldman, S. P., & Drake, G. W. F. 1981, Phys. Rev. A, 24, 183
Gu, M. F. 2003, ApJS, 589, 1085
Heger, A., Jeannin, L., Langer, N., & Baraffe, I. 1997, A&A, 327, 224
Houck, J. C., Bregman, J. N., Chevalier, R. A., & Tomisaka, K. 1998, ApJ, 493, 431
Immler. S., Pietsch, W., & Aschenbach, B. 1998, A&A, 331, 601
Immler, S., & Lewin, W. H. G. 2003, in Supernovae and Gamma-Ray Bursters, Lecture notes in physics, ed. K. W. Weiler (Springer), 598, 91
Innes, D. E. 1992, A&A, 256, 660
Itoh, H. 1981a, PASJ, 33, 1
Itoh, H. 1981b, PASJ, 33, 521
Itoh, H. 1986, PASJ, 38, 717
Itoh, H. 1988, PASJ, 40, 673
Iwamoto, K., Young, T. R., Nakasoto, N., et al. 1997, ApJ, 477, 865
Kaaret, P. 2001, ApJ, 560, 715
Kaastra, J. S., & Jansen, F. A. 1993, A&AS, 97, 873
Kifonidis, K., Plewa, T., Janka, H.-Th., & Müller, E. 2003, A&A, 408, 621
Kohmura, Y., Inoue, H., Aoki, T., et al. 1994, PASJ, 46, L157
Landi, E., del Zanna, C., Young, P. R., et al. 2005, ApJS, in press
Landini, M., & Monsignori Fossi, B. C. 1990, A&AS, 82, 229
Landini, M., & Monsignori Fossi, B. C. 1991, A&AS, 91, 183
Leising, M. D., Kurfess, J. D., Clayton, D. D., et al. 1994, ApJ, 431, L95
Lundqvist, P., & Fransson, C. 1988, A&A, 192, 221
Mazzotta, P., Mazzitelli, G., Colafrancesco, S., & Vittorio, N. 1998, A&AS, 133, 403
Meynet, G., & Maeder, A. 2003, A&A, 404, 975
Mewe, R 1999, in Lecture Notes in Physics, ed. J. van Paradijs, & J. A. M. Bleeker (Springer), 520, 109
Mewe, R., Lemen, J. R., & van den Oord, G. H. J. 1986, A&AS, 65, 511
Matzner, C. D., & McKee, C. F. 1999, ApJ, 510, 379
Michael, E. N., Zhekov, S., McCray, R., et al. 2002, ApJ, 574, 166
Müller, E. Fryxell, B., & Arnett, D. 1991, A&A, 251, 505
Nadyozhin, D. K. 1985, Ap&SS, 112, 225
Nahar, S. 1996, ApJS, 106, 213
Nahar, S. 1999, ApJS, 120, 131
Nahar, S., & Pradhan, A. 1997, ApJS, 111, 339
Nomoto, K., & Hashimoto, M. 1988, Phys. Rep., 163, 13
Nomoto, K., Iwamoto, K., & Suzuki, T. 1995, Phys. Rep., 256, 173
Panagia, N., Vettolani, G., Boksenberg, A., et al. 1980, MNRAS, 192, 861
Pequignot, D., Petitjean, P., & Boisson, C. 1991, A&A, 251, 680
Plewa, T. 1993, Acta Astron., 43, 235
Plewa, T. 1995, MNRAS, 275, 143
Plewa, T., & Różyczka, M. 1992, Acta Astron., 42, 295
Pooley, D., Lewin, W. H. G., Fox, D. W., et al. 2002, ApJ, 572, 932
Pooley, D., & Lewin, W. H. G. 2004, IAU Circ., 8390
Ray, A., Petre, R., & Schlegel, E. M. 2001, AJ, 122, 966
Raymond, J. C. 1979, ApJS, 39, 1
Ryder, S., Staveley-Smith, L., Dopita, M., et al. 1993, ApJ, 416, 167
Salasnich, B., Bressan, A., & Chiosi, C. 1999, A&A, 342, 131
Schlegel, E. M. 1995, Rep. Prog. Phys., 58, 1375
Schlegel, E. M., Kong, A., Kaaret, P., DiStefano, R., & Murray, S. 2004, ApJ, 603, 644
Shigeyama, T., & Nomoto, K. 1990, ApJ, 360, 242
Shigeyama, T., Suzuki, T., Kumagai, S., et al. 1994, ApJ, 420, 341
Shull, J. M., & Van Steenberg, M. 1982, ApJS, 48, 95
Sramek, R. A., & Weiler, K. W. 2003, in Lecture Notes in Physics, ed. K. W. Weiler (Springer), 598, 145
Sorokina, E. I., Blinnikov, S. I., Kosenko, D. I., & Lundqvist, P. 2004, Astron. Lett., 30, 737
Sutherland, R. S. 1998, MNRAS, 300, 321
Sutherland, R. S., & Dopita, M. A. 1993, ApJS, 88, 253
Sutherland, R. S., Bicknell, G. V., & Dopita, M. A. 2003, ApJ, 591, 238
Suzuki, T. 1994, Ph.D. Thesis, University of Tokyo
Suzuki, T., & Nomoto, K. 1995, ApJ, 455, 658
Swartz, D. A., Ghosh, K. K., McCollough, M. L., et al. 2003, ApJS, 144, 213
Tarter, C. B., Tucker, W. H., & Salpeter, E. E. 1969, ApJ, 156, 943
Uno, S., Mitsuda, K., Inoue, H., et al. 2002, ApJ, 565, 419
Verner, D. A., & Ferland, G. J. 1996, ApJS, 103, 467
Woosley, S. E., & Weaver, T. A. 1995, ApJS, 101, 181
Weiler, K. W., Sramek, R. A., van Dyk, S. D., & Panagia, N. 1993, IAU Circ., 5752
Young, P. R., Del Zanna, G., Landi, E., et al. 2003, ApJS, 144, 135
Zimmerman, H. U., Lewin, W., Predehl, P., et al. 1994, Nature, 367, 621
Zatsarinny, O., Gorczyca, T. W., Korista, K. T., Badnell, N. R., & Savin, D. W. 2003, A&A, 412, 587
Zatsarinny, O., Gorczyca, T. W., Korista, K. T., Badnell, N. R., & Savin, D. W. 2004a, A&A, 417, 1173
Zatsarinny, O., Gorczyca, T. W., Korista, K. T., Badnell, N. R., & Savin, D. W. 2004b, A&A, 426, 699